

## The MVACS Surface Stereo Imager on Mars Polar Lander

P. H. Smith, R. Reynolds, J. Weinberg, T. Friedman, M. T. Lemmon,  
R. Tanner, R. J. Reid, R. L. Marcialis, B. J. Bos, and C. Oquest

Lunar and Planetary Laboratory, University of Arizona, Tucson, Arizona

H. U. Keller, W. J. Markiewicz, and R. Kramm

Max Planck Institute for Aeronomy, Katlenberg-Lindau, Germany

F. Gliem and P. Rueffer

Technical University of Braunschweig, Braunschweig, Germany

**Abstract.** The Surface Stereo Imager (SSI), a stereoscopic, multispectral camera on the Mars Polar Lander, is described in terms of its capabilities for studying the Martian polar environment. The camera's two eyes, separated by 15.0 cm, provide the camera with range-finding ability. Each eye illuminates half of a single CCD detector with a field of view of 13.8° high by 14.3° wide and has 12 selectable filters between 440 and 1000 nm. The  $f/18$  optics have a large depth of field, and no focusing mechanism is required; a mechanical shutter is avoided by using the frame transfer capability of the  $528 \times 512$  CCD. The resolving power of the camera, 0.975 mrad/pixel, is the same as the Imager for Mars Pathfinder camera, of which it is nearly an exact copy. Specially designed targets are positioned on the Lander; they provide information on the magnetic properties of wind-blown dust, and radiometric standards for calibration. Several experiments beyond the requisite color panorama are described in detail: contour mapping of the local terrain, multispectral imaging of interesting features (possibly with ice or frost in shaded spots) to study local mineralogy, and atmospheric imaging to constrain the properties of the haze and clouds. Eight low-transmission filters are included for imaging the Sun directly at multiple wavelengths to give SSI the ability to measure dust opacity and potentially the water vapor content. This paper is intended to document the functionality and calibration of the SSI as flown on the failed lander.

### 1. Introduction

The Surface Stereo Imager (SSI) is part of the Mars Volatiles and Climate Surveyor (MVACS) integrated payload on the Mars Polar Lander (MPL) spacecraft; D. Paige is the Principal Investigator. It was launched on January 3, 1999, and landed but failed to function near 76°S and 195°W in polar layered terrain on December 3, 1999. The heritage of the SSI comes entirely from the Imager for Mars Pathfinder (IMP) on the Pathfinder mission [Smith *et al.*, 1997b; Reid *et al.*, 1999], of which it is intended to be an exact copy. Because it is such a close copy, extensive reference will be made to the Smith *et al.* [1997b] paper on the IMP camera.

Several changes were required to accommodate a new spacecraft design [Reynolds *et al.*, 2001]. The interface with the spacecraft has been changed to high-speed serial (RS-422) from Pathfinder's parallel (VME bus) interface, and the electronics have been compressed from three boards to two. The electronics were assigned double duty, also serving the Robotic Arm Camera (RAC), which is described separately [Keller *et al.*, this issue].

The mission goals for SSI include operational support for the robotic arm and its sample collection tasks for the Thermal and Evolved Gas Analyzer, another MVACS instrument

[Boynton *et al.*, this issue]. Operationally, the SSI stereoscopic imagery was designed to maintain a virtual environment needed to create command sequences for the arm and RAC. This range map can be augmented by RAC images in locations inaccessible to SSI, such as underneath the lander. Periodic images of the arm will serve to verify its true location compared to its commanded location. Images taken of the lander deck and solar panels will be valuable as troubleshooting guides when performance of various subsystems degrades.

The scientific objectives for SSI fall into several broad categories: geomorphology, mineralogy, and atmospheric studies. Geomorphology, as always, is governed by the choice of landing site. The polar layered terrain affords the rare opportunity to learn the stratigraphic history of this circumpolar geologic unit. Local landforms are likely to show fine-scale layering that is likely to have been depositional in origin, but later modified by strong winds. Unlike the Viking Landers 1 and 2 and Pathfinder sites, few, if any, rocks are expected. Defining the role of ices in the formation of the layers is a prime goal for SSI. To aid in the study of the layers, the camera's multispectral imaging mode will be used. Subtle color differences between layers may indicate a different ice fraction, changes in particle size, or composition changes. We will compare the spectra to those obtained at the distant Pathfinder site to check for variations in the globally distributed dust.

In addition to the stratigraphy we will look at local features to determine the topography and geology of the landing site, its

Copyright 2001 by the American Geophysical Union.

Paper number 1999JE001116.  
0148-0227/01/1999JE001116\$09.00

photometric characteristics, and its homogeneity over a wide range of spatial scales. The SSI will also search for long time-scale variations produced by atmospheric effects, for instance, aeolian modification of dune structures. In addition, it will observe effects resulting from the landing of the spacecraft and operations of the robotic arm and hence place constraints on the physical properties of the regolith.

By pointing the camera at the sky we can learn about the atmospheric haze and cloud properties. Images of the Sun through low-transmission, narrowband filters will be converted to optical depth measurements. Filters near the 935-nm water band allow us to constrain water vapor concentration. Sky brightness scans reveal the scattering phase function of the aerosols, which can in turn be analyzed to provide the size distribution, index of refraction, and shapes of the aerosols. Images of the sky also tell us about ice cloud formation and variability. As dust falls from the sky, the rate can be measured by the ratio of black to white targets. The magnetic strength of the dust will be measured on magnetic targets identical to those flown on Pathfinder [Madsen *et al.*, 1999].

The following pages describe the camera system and its calibrated properties. Then each experiment (panoramic imaging, stereoscopic imaging, mineralogy, and atmospheric studies) is individually discussed in terms of science goals, operations, and data analysis techniques.

## 2. SSI Description

Both the SSI and IMP were designed for a resolution of  $<1$  mrad/pixel, equivalent to the Viking cameras (color: 2.1 mrad/pixel, monochrome high-resolution: 0.7 mrad/pixel). The design specifications, nearly the same as previously described for the IMP camera [Smith *et al.*, 1997b], are summarized in Table 1. The focal plane array (FPA), supplied by the Max Planck Institute for Aeronomy (MPAe), has heritage from IMP and the descent imager (DISR) on the Huygens probe. Our decision to include stereo plus the requirement for low mass led us to split a single detector into left and right image areas and avoid the extra complexity of two separate focal planes. Therefore there are two identical  $256 \times 256$  pixel arrays, normally subframed to  $248 \times 256$  for each eye (Figure 1); each field of view (FOV) is  $13.8^\circ \times 14.3^\circ$ . Since the SSI is a copy of IMP, it maintains the same eye separation of 15.0 cm, and the light path is folded by two sets of mirrors to bring the light to the FPA. A drawing of the camera head is shown in Figure 2.

Early engineering trade-offs for IMP balanced the conflicting requirements of low mass and of high strength to survive the expected 100-*g* landing shock through the use of a challenging airbag-assisted bounce onto the surface of Mars. Titanium was used where possible because of its large strength-to-mass ratio. The gimbal is held with duplex bearing pairs that are dry-lubricated to maintain functionality at low temperature. Motor/gearhead combinations, supplied by the American Technology Consortium (ATC), are positioned along both the azimuth and elevation axes. The motors are four-pole steppers with an 81.3:1 gearhead ratio, giving a step size of  $0.553^\circ$ , and are driven at 10 steps/s; the step count from a hard stop is maintained in memory to determine position. The same principles have been applied to SSI except that more care has been taken to avoid backlash in the gearheads. The filter wheel motors are six-pole steppers with a 10:1 gearhead ratio, giving a step size of  $3^\circ$ , and are driven at 50 steps/s, which is equivalent to 5 filters/s.

**Table 1.** SSI Camera Specifications at  $-20^\circ\text{C}$

Specification	Value
<i>CCD</i>	
Readout noise	14.4 electrons
Full well	109,300 electrons
Readout time, s	2 for the full array, 1 for the left eye only
Exposure time	0–32.7 s; step size = 0.5 ms, autoexposure available
Spectral range, nm	440–1000
Gain	26.7 electrons/DN
A/D conversion	12 bits per pixel
Pixel size, $\mu\text{m}$	$23 \times 17.6$ for an antiblooming channel
<i>Optomechanical</i>	
Scale, mrad/pixel	
Left	0.975
Right	0.975
Focal length, f/#	23 mm, f/18
Field of view	$13.8^\circ \times 14.3^\circ$
Depth of field	Best focus: 1.3 m, DOF: 0.5 m to infinity
Filters per eye	12 (four are solar filters, one diopter lens (right eye) to view the Tip Plate Magnet)
Stereo separation, cm	15.0
Toe-in, mrad	
Left	18.1
Right	$-15.5$ , measured from EL axis
AZ/EL step size	$0.553^\circ$ , $1^\circ$ hysteresis (backlash)
Repeatability	$<4$ mrad, when approaching from the same direction
Step speed	10 steps/s ( $5.53^\circ/\text{s}$ )
Pointing range	full azimuth, $+90^\circ$ to $-67^\circ$ elevation

A mast, supplied by AEC Able Corp., of the open lattice type used by magnetometers is held in its stowed position during cruise by a fixed pin. About 15 min after landing on sol 0, the pyro-activated pin puller is fired and the camera pops up 62 cm above its stowed location (and 79 cm above the deck), about 1.6 m above the surface. From this vantage the horizon for a featureless sphere the size of Mars is 3.4 km away. Before deployment the camera is pinned in azimuth but will be able to take one vertical scan from the deck to above the horizon.

The primary area for stereoscopic imaging, to aid robotic arm operations with contour maps and distance information, is from 2–3 m from the camera. To balance this requirement with the desire for an accurate range map to 50 m, a toe-in of the fold mirrors of 18.1 mrad for the right eye and  $-15.5$  mrad for the left eye gives complete overlap of the left and right eyes at 4.46-m distance. The keystone distortion caused by this toe-in is judged not to be significant.

An intensive effort was made to reduce light scattering inside the camera head. A series of baffles, darkened with Martin Black, is used to reduce the stray light reflected off the side walls to about 1% per reflection. Martin Black is an anodizing process for aluminum developed at Lockheed Martin Astronautics that creates an extremely rough surface that is dyed black and sealed; the combination of surface roughness and dye provides greater absorption of UV, visible, and IR radiation than can be achieved with other available surface treatments. A knife-edge baffle reduces crosstalk between the left and right eyes to undetectable levels outside of a 12-pixel “dead” band. The outer windows are recessed in their housings until they

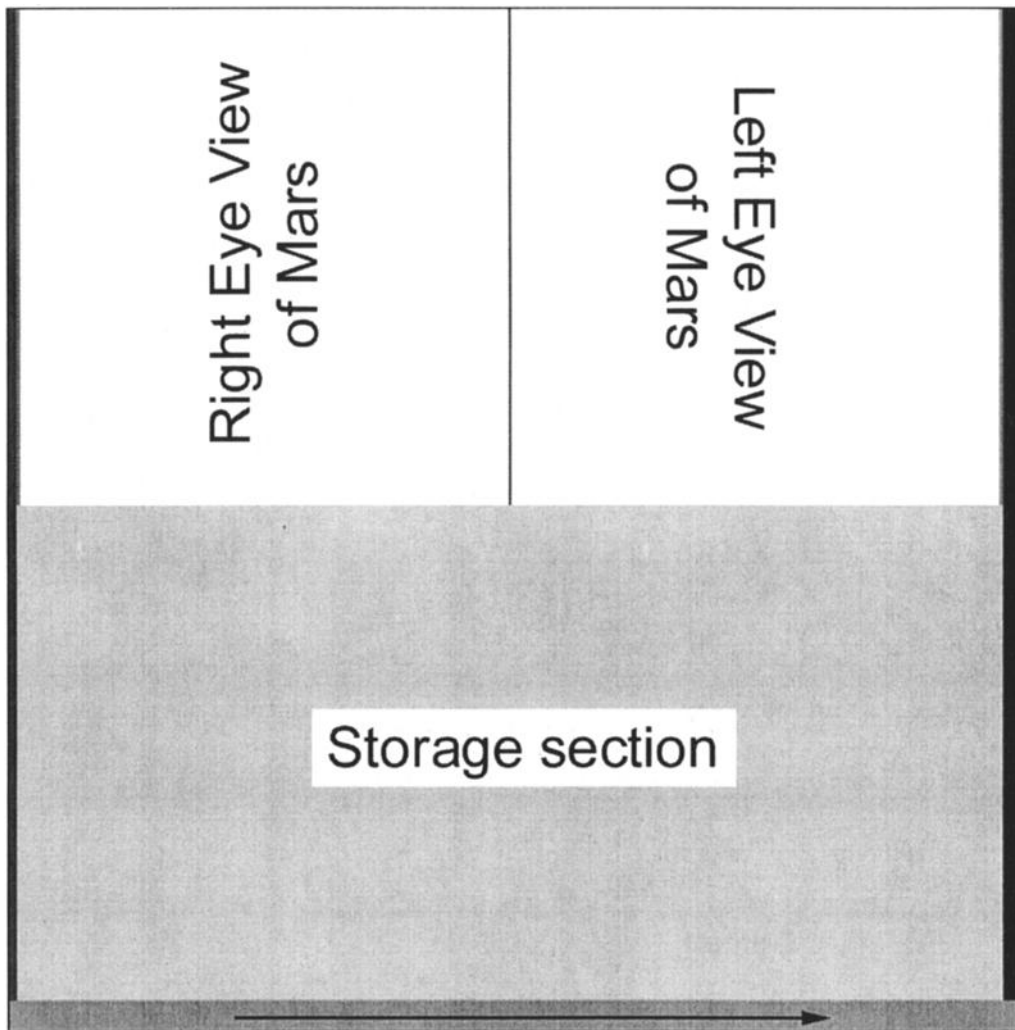


**Figure 1.** The areas on the Surface Stereo Imager (SSI) CCD are shown here. At the bottom is the horizontal readout register (HRR). Above that is the  $512 \times 256$  storage section, which is not exposed to light. At the top are two  $256 \times 256$  imaging areas; the two columns at both the extreme left and right are partially shaded "gray columns." At the left are the null pixels, 4 HRR pixels that are not connected to pixel columns; at the far right is another null strip. Next to the right null strip is an eight-column dark strip overcoated with Al. Image data are shifted down to the storage section and the HRR, then read out to the right one row at a time.

nearly touch the fold mirrors so that the housings act as sunshades to inhibit direct sunlight from scattering off dust particles on the windows; it also protects windows from falling dust.

There are two electronic boards housed in the Payload Electronics Box (PEB), where their environment is temperature controlled. The two boards mount to opposite sides of a thermal plate of aluminum that acts as a heat sink and support bracket. The detector cables from both the SSI and the RAC cameras connect to the CCD Readout Board (CRB) [Kramm, 1998] and the motor and auxiliary readouts connect to the Frame Buffer Board (FBB). The FBB interfaces to the spacecraft through its Payload and Attitude Control Interface (PACI) board with a 1-MHz serial link controlled by a Field Programmable Gate Array functioning as a state machine for command decoding. Other functions for the FBB are phasing the steps and driving the five (three for SSI, two for RAC) motors as well as turning on the RAC lamps.

The camera system is controlled through a sequence of up-

linked commands that are time tagged and stored in spacecraft RAM. The image command includes many optional parameters that control the exposure and processing. Everything from the exposure time to the amount and type of data compression is specified here and attached to the data set to be placed in the header. Subframing boundaries and pixel-averaging parameters can also be specified. After processing, the packetized images are stored in the telemetry buffer.

Several types of data compression are included in the SSI software package. Lossless compression (1.3:1 to 2:1, depending on the scene entropy) using the Rice algorithm developed at the Jet Propulsion Laboratory (JPL) gives the highest fidelity. Other methods of lossless compression include subframing the image. For instance, most pictures of the Sun taken through the solar filters will be returned as  $30 \times 30$  pixel blocks centered on the Sun image. Pixel averaging ( $m \times n$  pixels) can be used when full resolution is not needed. Row and column averages will be used for sky images; this gives the gradient and

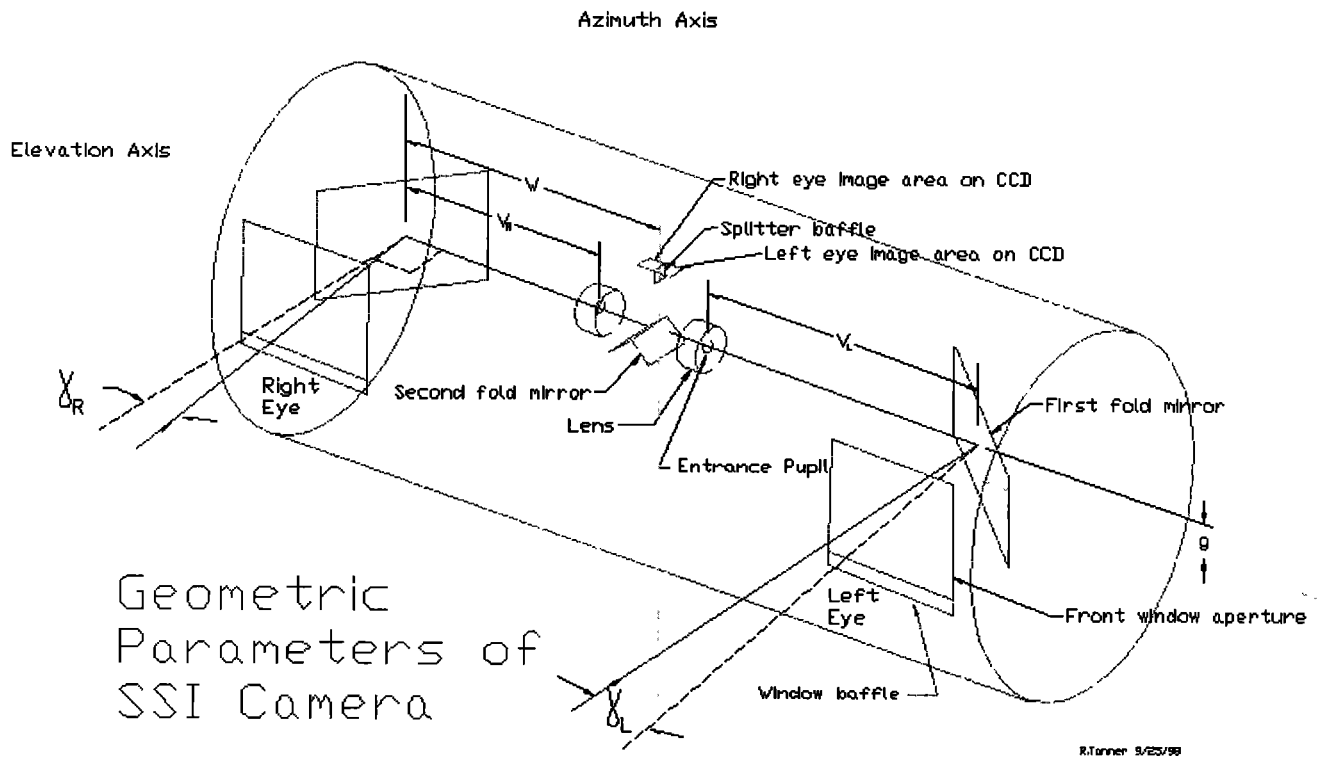


Figure 2. SSI optical diagram.

the edges of cloud features but not the high resolution of an image. These methods can be used in combinations for highest compression.

A modified JPEG compressor using arithmetic coding developed at the Technical University of Braunschweig in Germany will normally be used at ratios from 2:1 to 24:1. It is both enhanced by Local Cosine Transform prior to the JPEG-specific Discrete Cosine Transform and made robust against data dropouts [Rueffer *et al.*, 1995]. We have performed studies of compression using Pathfinder images that were downlinked with lossless compression. We found that the variations on standard JPEG compression performed similarly well; we have chosen the Arithmetic JPEG as a baseline. A sample of the performance is shown in Table 2 for an average of two scenes from the Pathfinder superpan containing a rocky foreground and some sky above the horizon. We also found that using pixel blocking, especially in conjunction with JPEG compression, substantially degrades performance relative to the same compression ratio with JPEG alone. Thus we do not recommend pixel blocking for flight use.

Prior to compression, a single-eye SSI frame contains  $248 \times 256 \times 12$  bits, or 762 kb. Downlinking the data "raw" (uncompressed) requires putting the 12-bit data into 16-bit words by adding 4 flag-bits, resulting in an effective compression ratio of 0.75:1 and a 1.00 Mb image. Both the lossy (JPEG) and lossless (Rice) compressors efficiently discard these extra bits, and compression ratios refer to the original 12-bit/pixel image (e.g., a 762-kb full frame compressed at 6:1 requires 127 kb of downlink). About 100 frames are combined into a monochromatic panorama, which brings the data volume to 76 Mb; instrument and packet headers add another 5% for a total of 80 Mb. A typical day on Mars allows the return of 30 Mb of SSI data.

Therefore compression is an indispensable tool for the early mission. A 6:1 compressed panorama has few artifacts, compresses to 13 Mb, and is easily returned during a single sol.

### 3. Laboratory Calibration

The SSI has been characterized and calibrated with respect to absolute responsivity, spectral response, image quality, flat fielding, stray light, and pointing accuracy. The primary calibration took place during November and December 1997, and the data set comprises  $\sim 3$  GB on optical disk storage (CD-ROM).

Table 2. Flight Software Arithmetic Compression<sup>a</sup>

Quality	Compression Ratio	RMS error, %
99	1.66	0.052
95	2.73	0.251
90	3.66	0.452
85	4.44	0.621
80	5.12	0.765
70	6.37	1.001
60	7.51	1.178
50	8.54	1.317
30	11.48	1.651
20	14.71	1.924
10	23.20	2.486
1	234.90	6.897

<sup>a</sup>The commanded quality factor, and the resulting compression ratios and errors, is averaged for two scenes. Note that the ratio and error will be scene dependent.

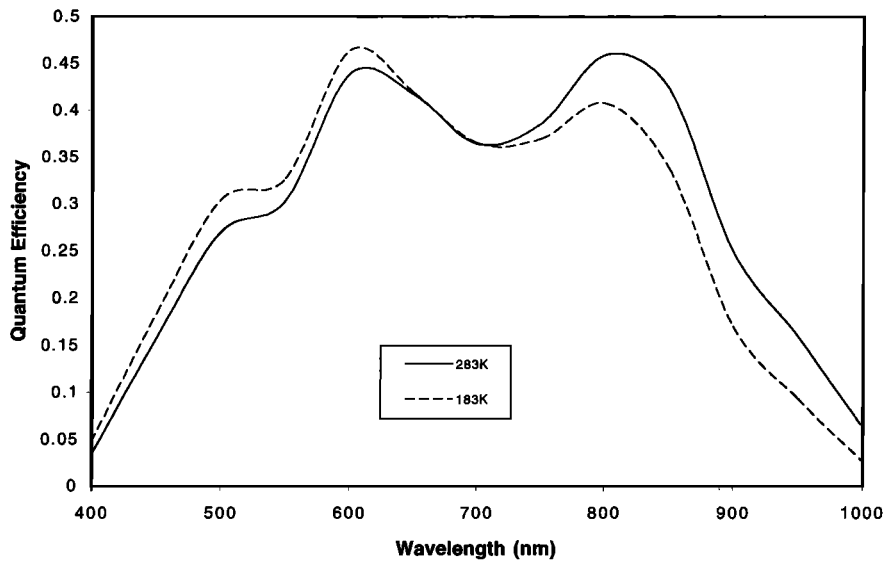


**Figure 3.** The CCD quantum efficiency is shown as a function of wavelength at two temperatures. The dotted curve is taken at  $T = 183$  K, and the solid curve is taken at 283 K. Because of the large change in quantum efficiency with temperature at wavelengths  $>800$  nm, a 2-W heater was added to the back of the CCD to stabilize its temperature at  $-20^{\circ}\text{C}$  or above.

### 3.1. CCD Properties

The SSI detector differs from that used by Pathfinder in at least one key aspect: the back side, or ground plane, has been coated with gold, not aluminum. A chemical reaction between the epoxy and the Al backing caused shifts in the ground plane potential for several batches of CCDs. This problem is corrected with a gold coating on the back plane. The CCD deviates from linearity by  $<1\%$ , and quantum efficiencies approach 50% at the peak, falling rapidly to zero near 400 and 1050 nm (see Figure 3). The electronics readout noise at cold temperatures (below  $-20^{\circ}\text{C}$ ) is about 14.4 electrons so that with a gain of 26.7 electrons/data number (DN) the system noise is typically 1 DN, where DN is the number of counts from the analog-to-digital converter (ADC). SSI is equipped with a 12-bit ADC to reduce quantization uncertainty, and shot noise will limit the signal-to-noise ratio (SNR) to values of 350 per pixel at a full exposure of 4095 DN. The antiblooming gates capture any overflow charge and are grounded to initiate an exposure while the frame transfer ends an exposure after a preset exposure time. After transferring an image to the storage section of the CCD in 0.5 ms, the pixel charges are converted and stored in the frame buffer at a rate of  $16 \mu\text{s}/\text{pixel}$  such that the readout takes 2 s. However, the next frame cannot be acquired until the image stored in the frame buffer is transferred across the serial link and stored in the spacecraft memory. Total time per image is about 20–30 s, depending on how busy the spacecraft computer is.

The dark current is modeled using the following equation:

$$\text{DN}(T, t, x, y) = A_D t e^{(B_D T)} D(x, y) + A_S e^{(B_S T)} S(x, y) + A_N e^{(B_N T)} + O,$$

where  $t$  is exposure time in seconds,  $T$  is temperature in  $^{\circ}\text{C}$ ,  $(x, y)$  is the pixel location, and the other letters represent measured coefficients. The first term accounts for the accumulation of thermal electrons during image acquisition. The second term accounts for the accumulation of thermal electrons dur-

ing readout. The third term accounts for the DN generated in the null pixels (extra serial register pixels with no connection to the pixel array), and the final term is the electronics bias, which prevents slight instrumental drift from causing an underflow during analog-to-digital conversion.  $D(x, y)$  and  $S(x, y)$  are normalized to a mean of 1 and show the spatial variation of the dark current. Coefficients for this equation can be found in Table 3.

The dark current generated when the CCD is above  $-20^{\circ}\text{C}$  is an important contributor to the image. A dark frame consists of a combination of a bias offset (9.2 DN), the noise generated in the readout process, and the dark current gathered during an exposure. Ambient temperatures on Mars will cause the temperature of the CCD to rise as high as  $-10^{\circ}\text{C}$ . The average total dark current from the CCD as a function of temperature for several integration times is shown in Figure 4. For Martian temperatures the average dark current should never exceed 100 DN; however, individual pixel values can be much larger for long exposure times.

The dark current from a “dark strip” of eight columns next to the left eye, shielded from light with an Al overcoat, is used to scale dark current corrections. Periodic dark frames are obtained by placing the camera in a stowed position, selecting a solar filter, and taking a full frame. These dark frames are then scaled to match the dark current of a later image using a

**Table 3.** Scalar Dark Model Parameters

Dark Model Parameter	Left Eye	Right Eye
$A_D$	5.446	5.510
$B_D$	0.105	0.108
$A_S$	4.769	5.139
$B_S$	0.105	0.104
$A_N$	0.836	
$B_N$	0.099	
$O$	9.23	

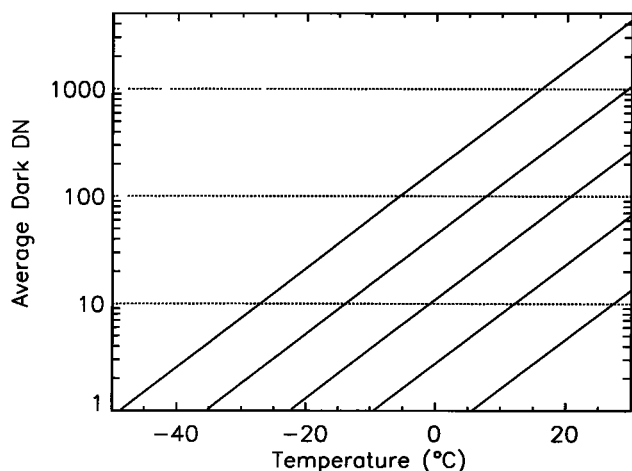


**Figure 4.** Average dark current accumulation in the active region of the CCD for five exposure times: from top to bottom, 32.7675 (maximum exposure), 8, 2, 0.5, and 0.1 s. Saturation is encountered at 4095 DN.

row-by-row ratio of dark strips. Care has been taken to correct for small light leaks into the “dark” strip.

### 3.2. Flat Fielding

Responsivity variations across the CCD array can be corrected (“flat fielded”), but the accuracy is limited by the noise in the image, by the compression factor used, and by imprecise knowledge of the CCD spatial response. The radiometric uniformity of our integrating sphere target is known only to  $\sim 1\%$ , which is the dominant limitation for removing SSI response variations. Earth-based flat fielding from laboratory measurements currently achieves this level of performance. Possible changes in the SSI spatial response pattern, particularly due to dust on the entrance windows, require subsequent calibration from images of the Martian sky.

The left and right eye filter 0 images of a uniform field are shown in Figure 5; both show the  $\cos^4$  (field angle) fall off that is characteristic of many imaging systems. The large spots are out-of-focus dust on various optical surfaces. Laboratory flat fields were generated by averaging 10 flat field images for each eye and filter and were corrected for bad pixels and known defects in the integrating sphere. Unlike the IMP flat fields, the SSI flat fields show no evidence of a cross-hatch pattern due to the manufacturing process. For in situ correction of responsivity variations, onboard flat field arrays were generated by averaging all geology flats (filters 0, 5–11) for each eye, excluding the Diopter filter (7R). This technique differs from that used for IMP [Smith *et al.*, 1997b], for which filter 0 responses were excluded.

### 3.3. Absolute and Relative Responsivity

The absolute responsivity of the SSI was calculated from laboratory measurements of the entire camera system after final assembly. The measurements were obtained by mounting the SSI in a thermal vacuum chamber equipped with antireflection-coated windows. Images were taken while the imager viewed a standard reflectance panel (spectralon) through the chamber windows at CCD chip temperatures of  $+25^\circ$ ,  $0^\circ$ ,  $-30^\circ$ ,  $-60^\circ$ , and  $-100^\circ\text{C}$ . The panel was illuminated normally by a standard lamp calibrated at a distance of 0.50 m. Figure 6 shows a schematic of the test setup.

Using the assumption that the panel was Lambertian, the panel spectral radiance was calculated using the relation

$$L_\lambda = \rho_\lambda E_\lambda / \pi, \quad (1)$$

where  $L_\lambda$  is the panel spectral radiance,  $\rho_\lambda$  is the panel spectral reflectance, and  $E_\lambda$  is the lamp spectral irradiance at 0.500 m. The loss of transmission through the chamber windows was corrected using measurements taken with and without the windows in place. The increased radiance of the reflectance panel due to reflections from stray light within the room was also corrected. We accomplished this by subtracting the SSI pixel

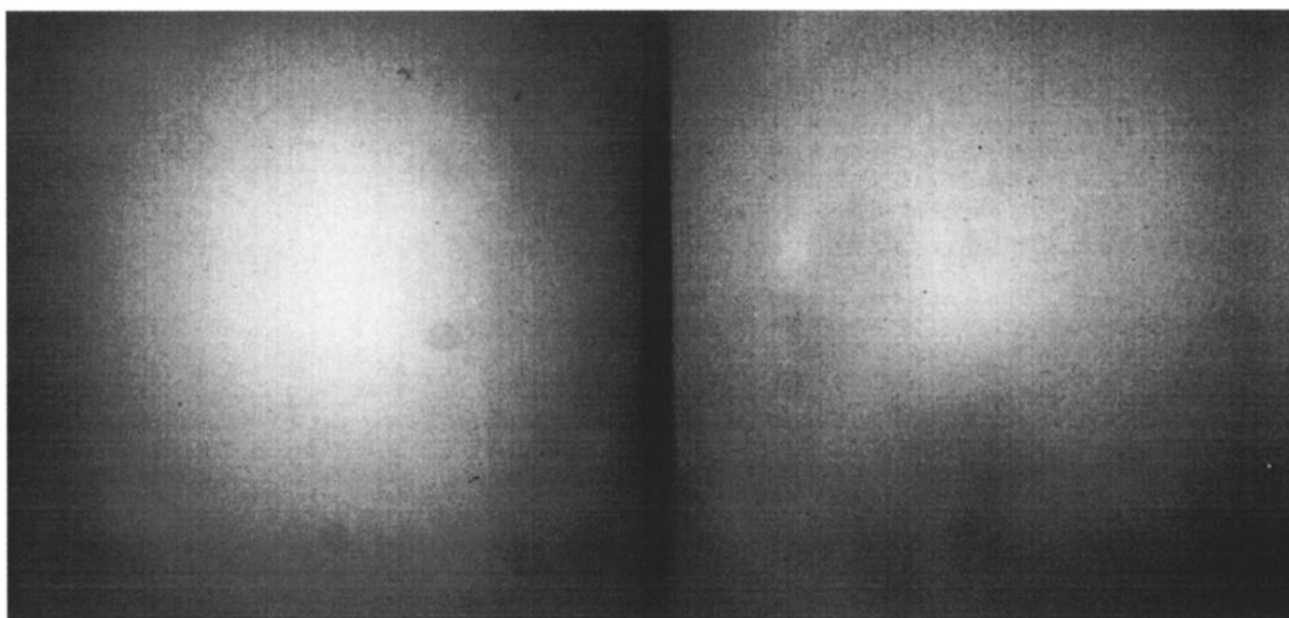


**Figure 5.** Histogram-equalized left and right eye filter 0 (443-nm) ground flat fields. Note falloff in response from the center of the optical axis outward, and out-of-focus dust on the optics.

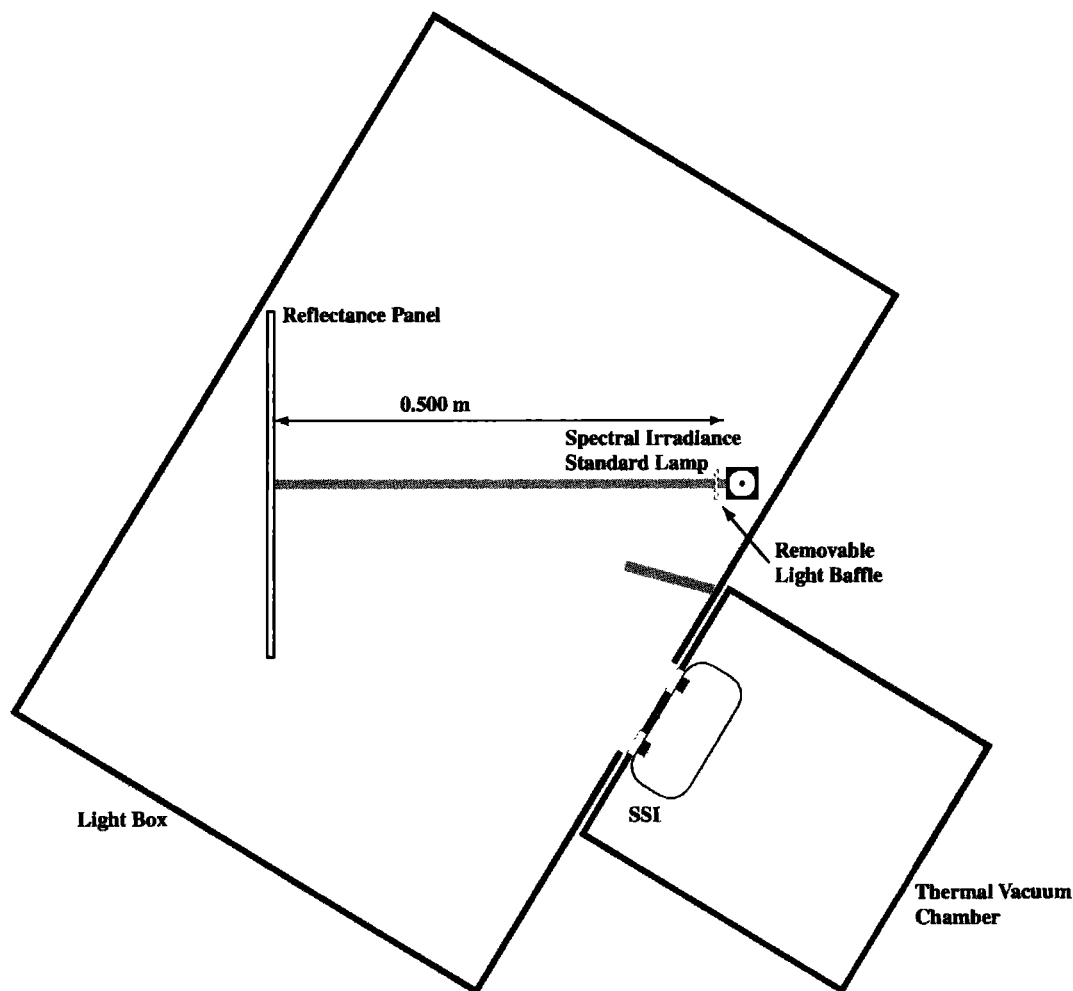


Figure 6. The laboratory setup for the measurement of absolute responsivity.

response, as the panel was being shadowed by a movable baffle, from the pixel response when the panel was fully illuminated. And, finally, the images were corrected for dark current and the camera's shutter effect so that after dividing the images by exposure time the pixel response (in units of DN/s) was proportional to the panel radiance. The average DN/s values from the central  $10 \times 10$  pixels of each eye were used in the calculations. The average pixel values were then divided by the calculated spectral radiance of the illuminated panel at each filter's ambient temperature central wavelength to obtain the absolute responsivity curves shown in Figure 7. A second-degree polynomial works well to fit the responsivity versus temperature; polynomial fits for all of the geology filters are shown in Table 4.

The SSI responsivity is less than that of IMP, primarily owing to a smaller pupil. At the shorter wavelengths, responsivity decreases as the temperature rises; the opposite is true at longer wavelengths. The responsivity is almost constant with temperature at intermediate wavelengths.

There are a number of error sources that combine to reduce the absolute calibration accuracy of the instrument. The major inaccuracies are lamp drift from its calibration radiance, distance errors from the lamp to the spectralon, improperly corrected stray light, and temperature mismeasurement. The lamp is reported to be calibrated to 2% by the National Institute of

Standards and Technology (NIST) laboratory, and the distance was measured to within a millimeter, giving a potential 2% error. Adding the errors from other sources, the total is <5% for known systematic errors. However, the instrument will drift somewhat during the 2 years from calibration to its landing on Mars, and a safer number is 10%.

We also performed a CCD heater test with an experimental setup similar to that used for absolute radiometry and include the results from that test in Figure 7 for comparison. The data points from the absolute tests were not part of the polynomial fit calculations, but their agreement with the fits is quite good.

Besides the absolute spectral response, the relative spectral response is important. Using a monochromator, each filter in Table 4 was scanned. To correct for the monochromator output profile, a standard detector was employed to trace out its spectral irradiance. The filter tracings corrected for the monochromator profile are shown in Figure 8a: each has been normalized to 1 at its peak.

Table 5 lists the absolute responsivities for each of the solar filters at a temperature of 23°C along with the temperature slope. A solar filter is typically 5 nm in bandwidth (see Figure 8b) with a transmission of  $\sim 0.1\%$ ; it is used to image the solar disk and obtain integrated disk measurements as a function of elevation angle. Some of the filters fall within the 938-nm water band and are used to measure water vapor.

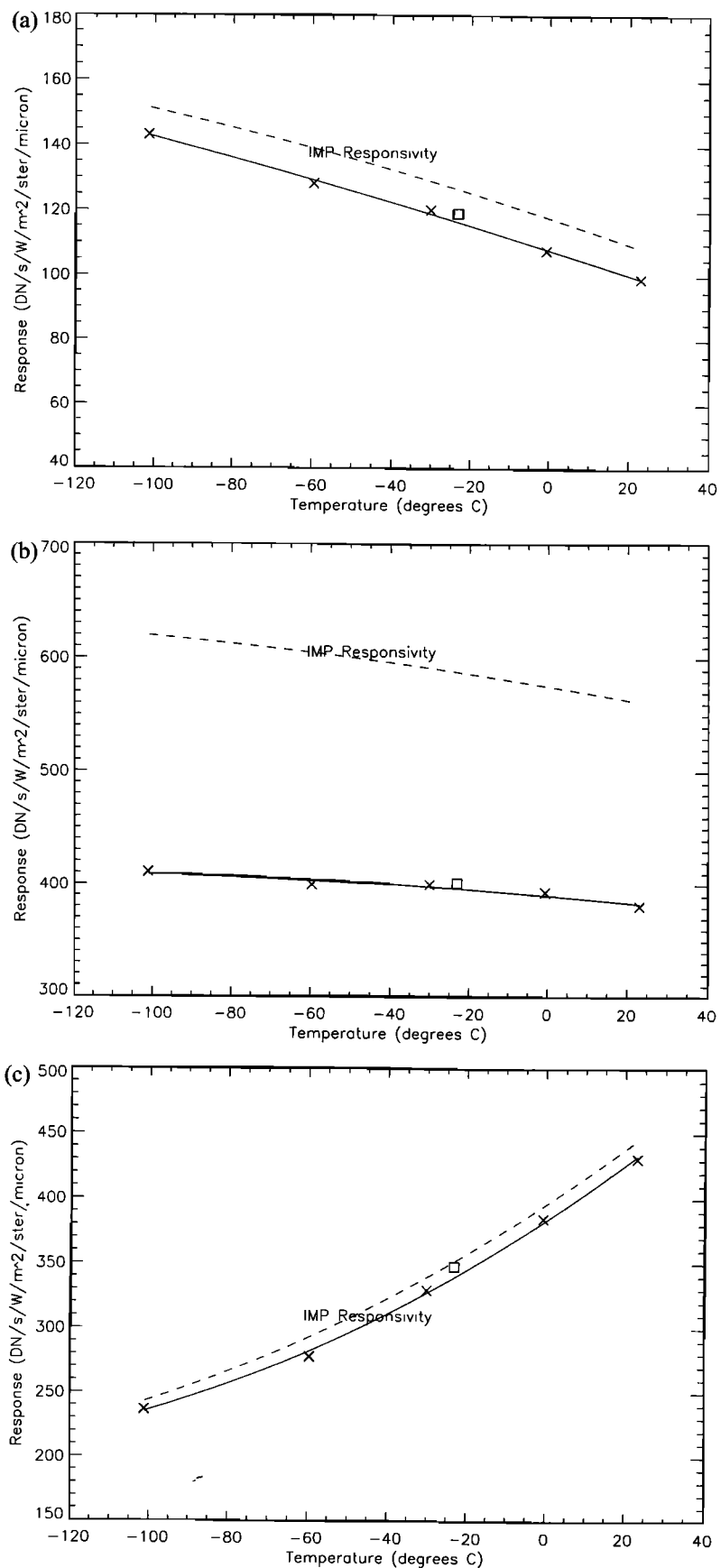


**Figure 7.** Responsivity versus temperature curves for three of the SSI geology filters (left eye filters (a) 0, (b) 5, and (c) 11). The “X” data points indicate the data used in the polynomial fit (solid line). The square data points were from CCD heater testing and were not included in the fit. Similar fits for IMP are shown as the dashed lines.

**Table 4.** Geology Filters and Their Responsivities<sup>a</sup>

Filter	Center Wavelength, nm	Bandwidth, nm	Responsivity $R_{02}$ (DN/s) $(\text{W/m}^2/\text{sr}/\mu\text{m})^{-1}$	Temperature Slope $M_1$ , $^{\circ}\text{C}^{-1}$	Temperature Curvature $M_2$ , $^{\circ}\text{C}^{-2}$
L0	445.3	23.6	107.97	$-3.49\text{E}-03^{\text{b}}$	$-2.96\text{E}-06$
L5	672.1	18.0	390.21	$-7.41\text{E}-04$	$-2.56\text{E}-06$
L6	802.4	20.8	711.83	$1.08\text{E}-03$	$1.01\text{E}-06$
L7	860.5	35.9	1246.3	$1.95\text{E}-03$	$2.75\text{E}-06$
L8	900.5	43.5	1032.4	$2.91\text{E}-03$	$5.97\text{E}-06$
L9	932.0	26.6	482.27	$4.09\text{E}-03$	$1.05\text{E}-05$
L10	1001.	26.5	160.66	$7.37\text{E}-03$	$2.25\text{E}-05$
L11	966.8	30.6	383.33	$5.30\text{E}-03$	$1.46\text{E}-05$
R0	445.9	22.6	71.168	$-3.40\text{E}-03$	$-3.51\text{E}-06$
R5	672.2	20.0	379.23	$-5.39\text{E}-04$	$-2.98\text{E}-06$
R6	752.9	18.8	424.42	$-3.36\text{E}-05$	$-4.85\text{E}-06$
R8	604.0	16.0	478.64	$-1.27\text{E}-03$	$-3.18\text{E}-06$
R9	533.3	28.0	445.49	$-1.92\text{E}-03$	$-6.71\text{E}-06$
R10	485.1	23.1	198.13	$-2.44\text{E}-03$	$-9.54\text{E}-06$
R11	966.4	30.8	359.12	$5.18\text{E}-03$	$1.30\text{E}-05$

<sup>a</sup> $T = 23^{\circ}\text{C}$  for wavelength and bandwidth. Responsivity as a function of temperature is  $R(T) = R_0 \times (1 + M_1 \times T + M_2 \times T^2)$  for  $T$  in  $^{\circ}\text{C}$ .

<sup>b</sup>Read  $-3.49\text{E}-03$  as  $-3.49 \times 10^{-3}$ .

### 3.4. Image Quality

The image quality of the Cooke triplet lenses has been quantified through calibration of the final SSI assembly. Geometric distortion is unmeasurable across the field of view (below 0.05 pixel). The line spread functions (LSF) and modulation transfer functions (MTF) also do not vary significantly over the field of view. See Figure 8 for typical LSF and MTF curves. The LSF broadening in the longer wavelength filter seen in Figure 9a is attributed not only to the increased diffraction blur of the lens but increased pixel crosstalk as well. We attribute the larger pixel crosstalk to the increased transparency of silicon to photons at longer wavelengths.

The MTF measurements (Figure 9b) illustrate that the SSI imaging system exhibits significant aliasing; that is, the CCD undersamples the higher spatial frequencies passed by the system. The combination of diffraction blur and electron crosstalk makes aliasing less significant at longer wavelengths. This is a primary reason for including the 965-nm stereo pair in the filter selections. The 965-nm wavelength will be used for the highest-precision stereo-ranging measurements because it causes the least systematic error at sharp edges.

We have developed a point spread function (PSF) model for the SSI similar to the one created for the IMP [Reid *et al.*, 1999] using the LSF/MTF calibration measurements. This model includes the diffraction blur due to the lens, the lens defocus, and the pixel response. The pixel response includes electron crosstalk effects as a function of wavelength. This model will allow us to accurately deconvolve the PSF from the SSI images effectively removing image blur.

### 3.5. Stray Light

The term “stray light” includes at least three components. The first component is a general “fogging” of the image due to scattering by dust particles on the optical surfaces. The second component is ghost images caused by multiple reflections within the camera optics. The third comes when bright objects outside the field of view (FOV) scatter light off the walls and other structures inside the camera in such a way that a false background pattern is added to the scene.

The stray light was measured by observing a collimated

beam on-axis and successively more off-axis to determine the contribution to the image from sources outside the FOV. The angular size of the source was 6 mrad, the size of the solar disk as seen from Mars. Several exposure times were used to increase the effective dynamic range. Measurements with the source inside of the FOV (see Figure 10) indicate that the scattered light 35 pixels from a solar-disk-sized image drops by a factor of  $10^4$ . Measurements with the source outside the field show a drop of  $10^5$ . By integrating the spot over the  $7^{\circ}$  field of the camera, we calculate that a dark rock shadow would receive  $\sim 1.5\%$  scattered light contribution from within the FOV. An additional 3–4% would come from light outside the FOV.

Ghost images of the bright source were also observed, with the first ghost having  $<0.1\%$  the brightness of the primary source. Ghost images will rarely be an issue (much less discernible) except when imaging the Sun.

### 3.6. Pointing Accuracy

The SSI has azimuth and elevation axes driven by four-pole stepper motors with planetary gearhead reducers (81.3:1); a single step produces  $0.553^{\circ}$  of motion. Low and high mechanical hardstops bound the range of motion of the camera head to full ranges of  $355.6^{\circ}$  in azimuth and  $180.9^{\circ}$  in elevation. Science operations on Mars do not require higher pointing accuracy, only the ability to subframe objects within the field with confidence. Azimuth and elevation backlash are better understood for SSI than for IMP and have been decreased to about  $\pm 0.5^{\circ}$  by decreasing play in the gearboxes. Figure 11 shows the azimuth backlash, and Figure 12 shows the elevation backlash. Backlash shows up as hysteresis between clockwise and counterclockwise motions. It is influenced by cable drag, so the increasing cable stiffness with decreasing temperature is an important factor. The azimuth backlash is well determined, while the elevation backlash has a step discontinuity about halfway through its travel that is subject to poor repeatability, especially following an increase in motor steps.

Camera pointing works best when simple rules are followed. When powered on, the camera must have absolute hardware initialization commanded to reset the camera to zero motor steps at the hardstop position; otherwise, camera pointing may

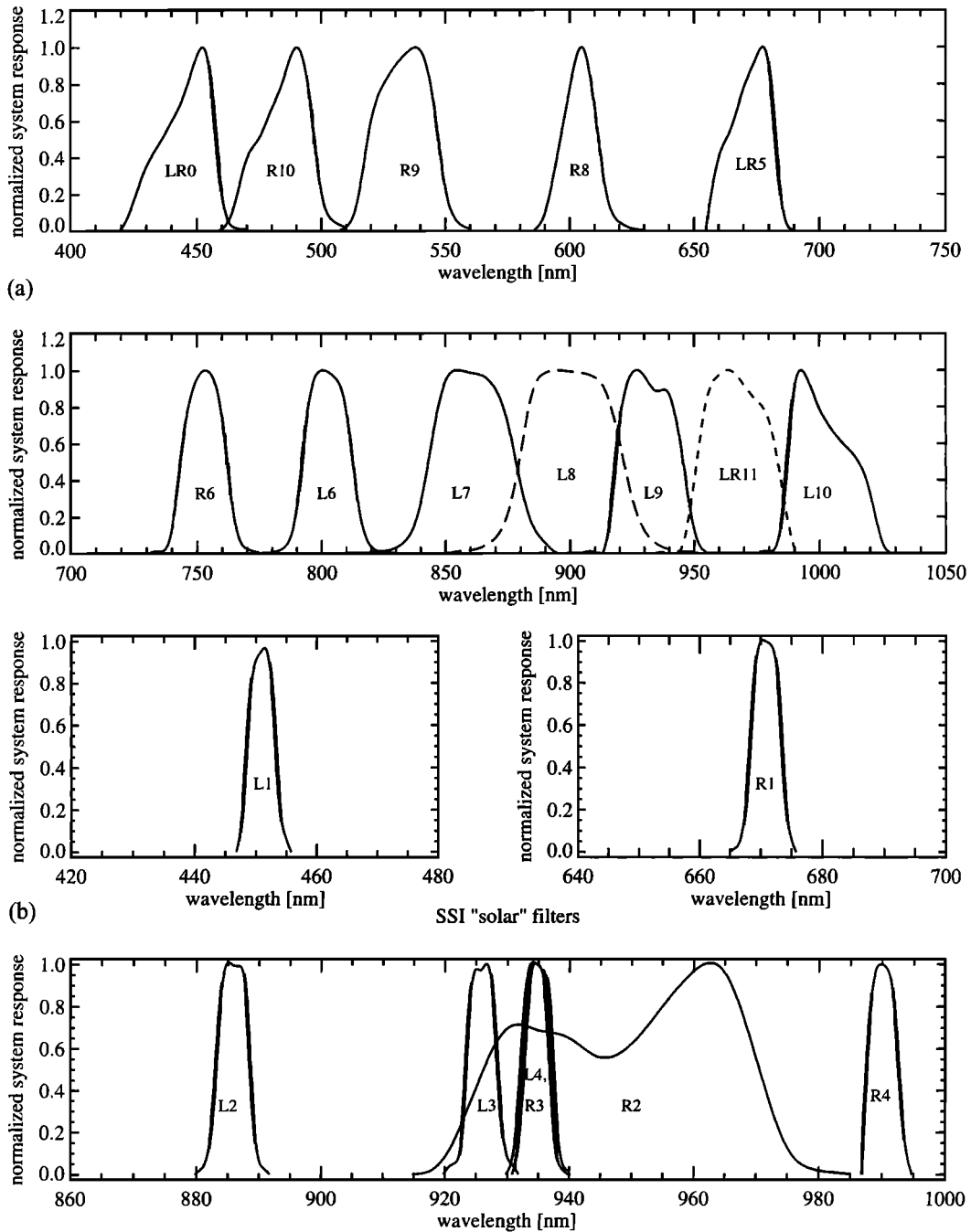


**Figure 8.** (a) Geology filter relative spectral response at  $T = -20^{\circ}\text{C}$  for all 12 filters listed in Table 4. (b) Solar filter profiles for the filters in Table 5.

be unknown. For incremental moves, those attempted without resetting the step counter, anytime a motor must reverse its direction there should be a move added to ensure that the cables have been dragged enough in the new direction to preload the axis. For example, to take a vertical column of images from upper to lower as part of a panorama, the camera should be commanded to a position above the first image position by at least 80 steps. Then as the column is exposed image by image, the backlash will be preloaded the same way for each image.

Single-step movements of the motors are not guaranteed to produce motion, since the backlash in azimuth and elevation is

slightly larger than a motor step. A two-step command,  $1.106^{\circ}$ , is the smallest increment that will reliably produce motion.

When subframing around a given target, the minimum rectangle enclosing the target should be increased by  $\pm 4$  pixels on the  $X$  axis and by  $\pm 8$  pixels on the  $Y$  axis to account for the worst case backlash. If JPEG compression is being used, care should be taken to ensure that the resulting  $X$  and  $Y$  image dimensions are divisible by 8, the block size used in the discrete cosine transform.

If these pointing rules are followed, and the camera model is used to compensate for backlash, then the pointing of the SSI

**Table 5.** Solar Filters and Their Responsivities<sup>a</sup>

Eye, Filter	Center Wavelength, nm	Bandwidth, nm	Responsivity $R_0$ , (DN/s) $(\text{W/m}^2/\text{sr}/\mu\text{m})^{-1}$	Temperature Slope $M_1$ , $^{\circ}\text{C}^{-1}$
L1	450.9	4.9	0.0386	-5.44E-03
L2	885.8	5.7	0.203	3.00E-03
L3	926.0	5.3	0.08176	5.01E-03
L4	935.0	4.9	0.32055	4.62E-03
R1	670.8	5.4	0.03053	-2.62E-03
R2	949.6	37.0	0.37185	5.70E-03
R3	934.5	4.9	0.32038	6.06E-03
R4	990.2	5.0	0.0256	8.20E-03

<sup>a</sup> $T = 23^{\circ}\text{C}$  for wavelength and bandwidth. Responsivity as a function of temperature is  $R(T) = R_0 \times (1 + M_1 \times T)$  for  $T$  in  $^{\circ}\text{C}$ .

can typically be determined to  $<2$  pixels in azimuth and  $<4$  pixels in elevation. This is a significant improvement over the 5-pixel uncertainty of IMP [Smith *et al.*, 1997b].

### 3.7. Color Imaging

Color imaging is an important SSI task. The SSI makes color images in one eye from red, green, and blue filters. Stereo color images will be made using the RGB information from one eye in combination with RB information in the other eye to deduce RGB for that eye. This method frees one of the RGB stereo pair filters in one eye to create an IR stereo pair at 965 nm for reduced aliasing in stereo-ranging measurements.

The feasibility of synthesizing green in one eye from red and blue was established during the Pathfinder mission [Maki *et al.*, 1999]. True color comes in two varieties on a Mars mission: Mars color and Earth color (the color Mars objects would have

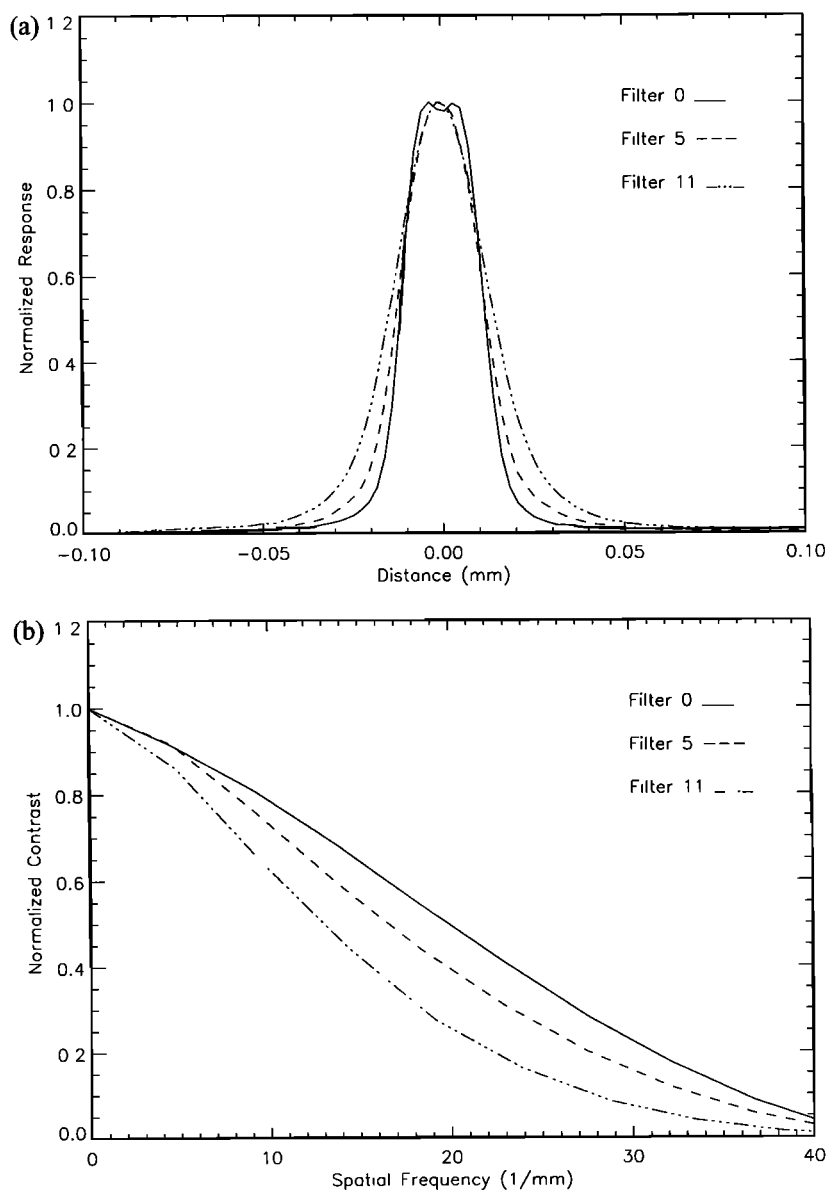


**Figure 9.** (a) The measured line spread function of the SSI system and (b) the SSI system modulation transfer function calculated from the Fourier transform of the line spread function.

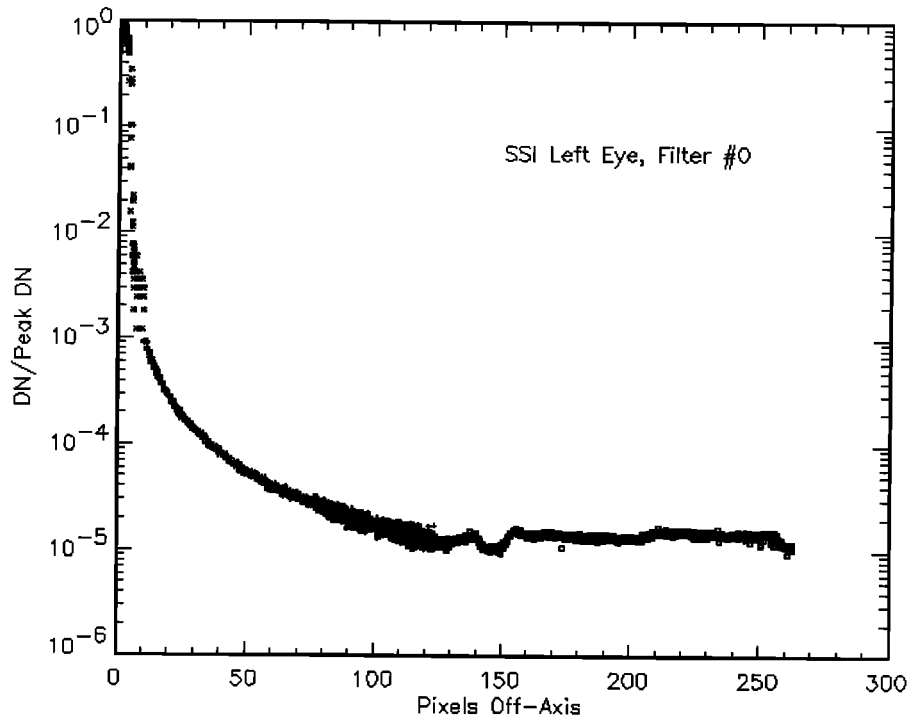


**Figure 10.** Stray light for filter L0. The general falloff with pixels off-axis is similar for all filters. Ghosts (such as the bumps near 135 and 160 pixels) vary from filter to filter.

if transported to the Earth). Either “true” color can be created in principle by using the absolute spectral calibration and an accurate sky illumination model. A relative method will also be available using images of the color targets on the lander deck.

The atmosphere of Mars can produce a family of true Mars colors due to the variation in the amount of dust reddening of the solar illumination and the significant contribution of the sky flux [Thomas et al., 1999].

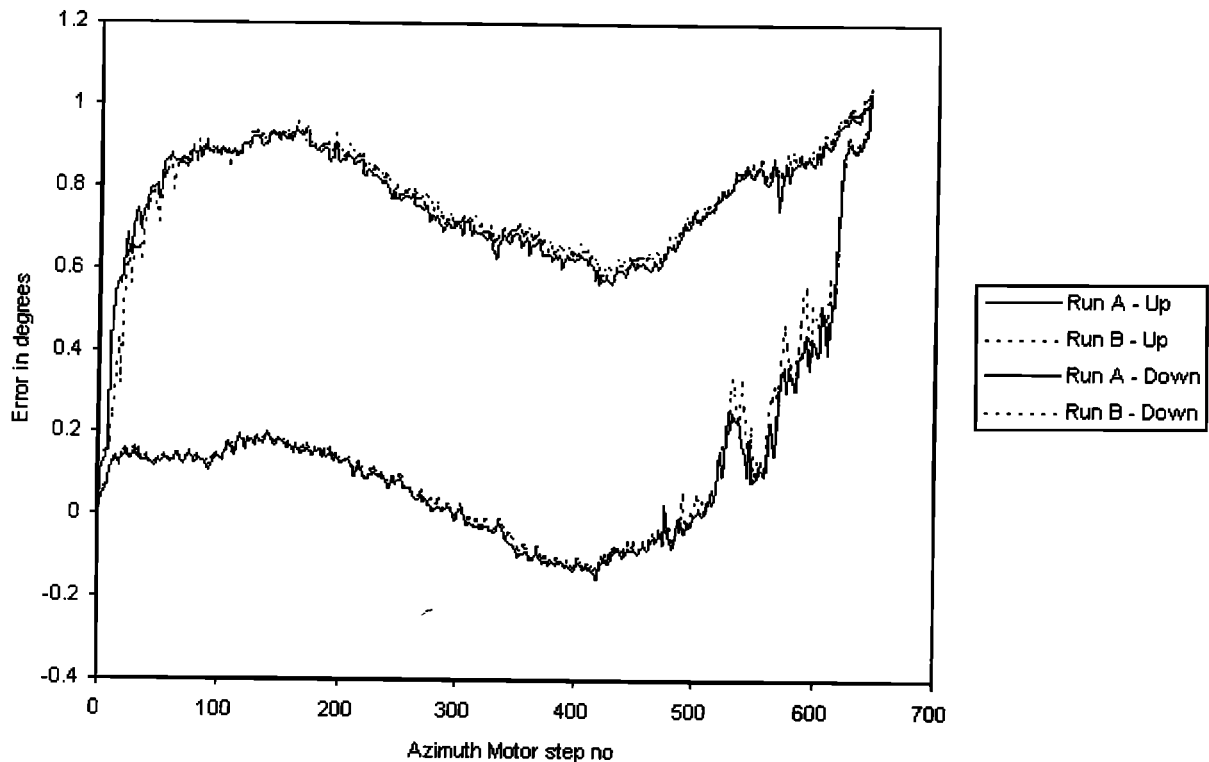


**Figure 11.** Azimuth backlash. Two data sets showing backlash for increasing (top curves) and decreasing (bottom curves) are shown.

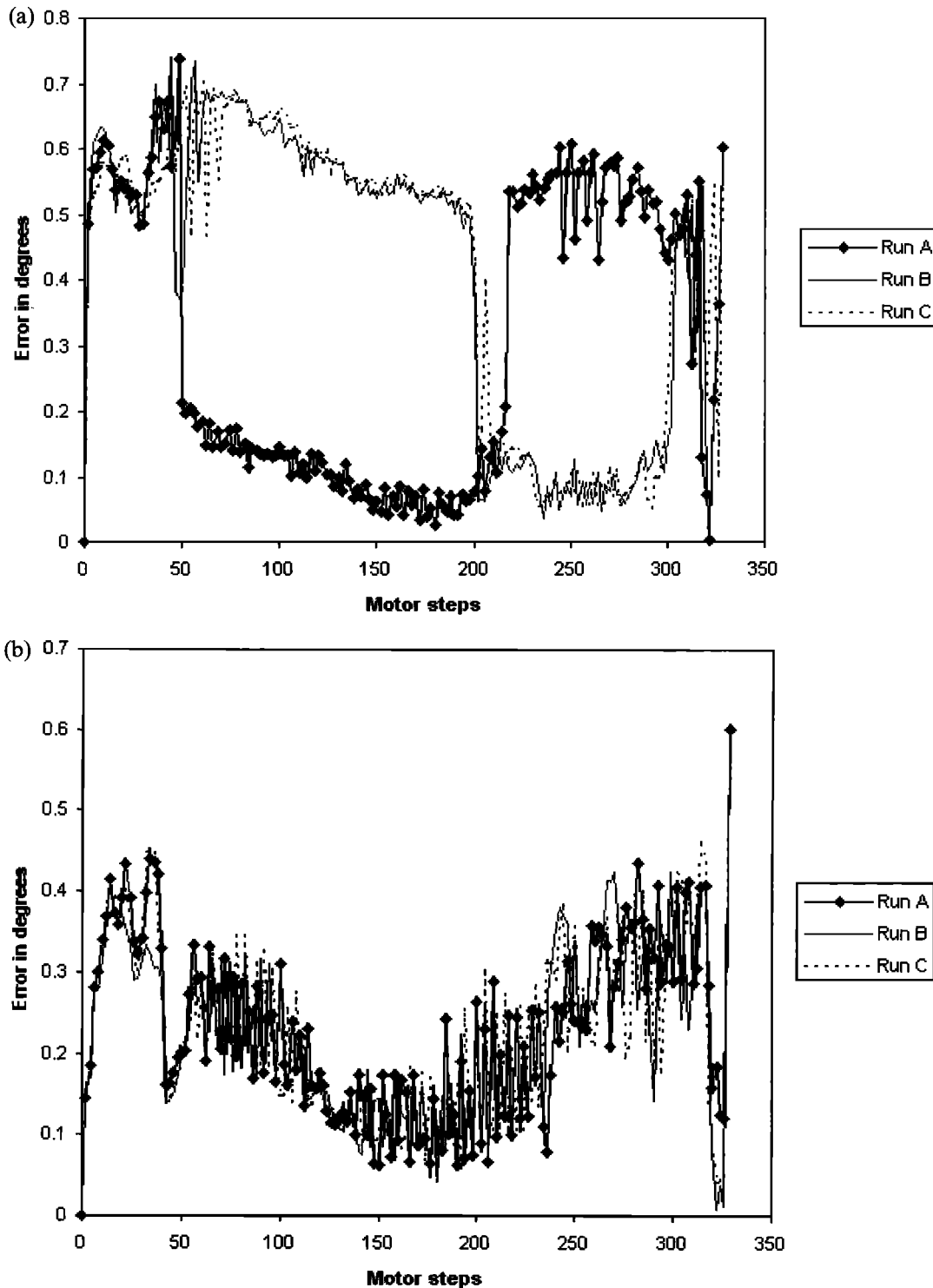


Figure 12. Elevation backlash. Three data sets for (a) increasing and (b) decreasing motor steps are shown.

### 3.8. Image Calibration

SSI images will be calibrated by a combination of flight software (FSW) aboard the spacecraft and ground software (GSW) after the data have been downlinked. Both types of calibration software derive from those used for IMP.

The SSI detector is nearly blemish-free, yet some pixels behave differently than the others; we call pixels outside the normal range "bad pixels." Pixels are bad if they fall outside of the 2.5-sigma value in an image of a flat field. A second way

that they can be flagged is they exhibit nonlinear behavior above the 1.6% level. FSW bad pixel correction eliminates spatial transients that adversely affect lossy (e.g., JPEG) image compression by replacing the value from a bad pixel with the value from an adjacent good pixel using a look-up table. The flight bad pixel table contains 881 left-eye and 889 right-eye bad pixels, although only 5 left-eye and 11 right-eye bad pixels exist inside a 2-pixel-wide border around the CCD.

The FSW will be used for electronic shutter correction, dark

current correction, and flat field removal. Electronic shutter correction removes the smearing caused by the 0.5-ms frame transfer as well as the dark accumulation during the 2-s read-out. This is the best way to remove shutter dark, electronic shutter smear, and hardware offset, but it does require an additional zero-time exposure to be subtracted from the image. This zero-time exposure adds about 30 s to the time required to take the image owing to the frame and serial link transfers.

Dark correction is performed by subtracting a dark pattern generated during laboratory calibration scaled by the average dark accumulation in the dark strip. This is generally not recommended, since light leaks onto the dark strip from the active region of the CCD can lead to incorrect estimates of total dark current. Dark correction is generally reserved for GSW.

Flat fielding is performed by dividing the image by the laboratory measured flat field pattern of the CCD. For FSW, owing to storage space limitations on the spacecraft, flat field patterns for all filters are averaged together, resulting in a single flight flat field pattern for each eye. As such, flat field correction is generally left to GSW, which uses the appropriate pattern for each filter, resulting in greater accuracy. In flight, it will be useful when extremely large compression ratios are commanded, and it will decrease the entropy of the scene, particularly the sky.

The ground software (GSW) calibration algorithms derive directly from those used for the final IMP calibration algorithms, as discussed by *Reid et al.* [1999]. The algorithms correct for dark current (from active, shutter, and null CCD regions), electronic shutter smearing, hardware and software DN offsets, bad pixels, and flat fields. The final step converts the image into radiance units.

The GSW algorithm applies corrections if they are not already performed by flight software. The ground bad pixel table contains 119 pixels for the left eye and 269 pixels for the right eye. Most are in the periphery of the CCD, with only 3 left-eye and 8 right-eye pixels outside a 2-pixel border at the edge of the CCD. These bad pixels are corrected by replacing the bad pixel with an adjacent good pixel using a look-up table generated during instrument calibration.

The SSI electronics add an additional 9.23 DN hardware offset to all image data. If not corrected by FSW, it is subtracted from the image data unless FSW shutter, dark, or flat correction is performed. This is checked during the mission with the null pixels taken at temperatures less than  $-20^{\circ}\text{C}$  where the thermal contribution is near zero. If any corrections (except bad pixel) were performed in FSW, an additional 16 DN were added to each image to prevent underflow in later processing. This software offset is subtracted when required.

Dark current (DN due to thermal generation of electron on the CCD) consists of three components, which are removed in turn. The smallest component is the null dark, a small thermal bias term (typically  $<1$  DN) that is subtracted. Shutter and active region dark are removed by subtracting a two-dimensional (2-D) dark pattern scaled by temperature from each image, using the dark model described above. The 2-D dark pattern will be updated using dark frames acquired during cruise and on Mars. For most observations on Mars, the contribution of dark current will be small but does become significant for long exposure time when the CCD is relatively warm.

If shutter correction is not performed in FSW, in addition to the shutter dark removed above will be a smearing effect caused by the 0.5-ms frame transfer. The smear is a small effect for exposure times  $>50$  ms. While small ( $<10$  DN for expected

Mars surface reflectance, i.e.,  $<0.5\%$  worst case), this effect can be corrected analytically, provided that the images contain pixels in the row closest to the storage region of the CCD (the only row not affected by smearing).

Laboratory flat fields for all solar and geology filters were obtained during instrument calibration as described above. If flat field correction was not performed by FSW, then it is performed by GSW by dividing the image DN by the 2-D flat field pattern. GSW flat field correction improves pixel-to-pixel responsivity variations to  $\sim 1\%$ .

Finally, the absolute responsivity of the system at the given eye, filter, and temperature is calculated. The corrected DN is divided by the exposure time and by the responsivity to convert each pixel value into intensity units ( $\text{W m}^{-2} \mu\text{m}^{-1} \text{sr}^{-1}$ ), with an absolute uncertainty of  $\sim 5\%$ . Before division the responsivity must be corrected to the proper temperature as measured at the CCD; see Table 4. This final step can be performed only by GSW.

#### 4. Color Panoramic Images

Before discussing the panoramic images, a brief review of the surface operations is helpful. The first camera operation is a vertical scan at a single azimuth. An azimuth panorama cannot be done prior to deploying the camera mast: a pin holds the camera head in azimuth. SSI executes a vertical scan sequence in five colors (L0 and R0, R9, L5 and R5, L8, and R8; see Table 4 for filter information) to image the Martian landscape. Immediately afterward, the mast is deployed. On sol 0 several engineering images are obtained (verifying deployment of the solar panels and the meteorology mast, checking the visible footpad, etc.). In addition, a 30-image red-filter panorama of the horizon, four vertical swaths of images (north, east, south, and west), and a red-stereo panorama of the prime workspace of the robotic arm will be obtained. On sol 1 a color panorama to the southeast will be obtained, and on sols 2 and 3 a color plus red-stereo panorama of the entire landing site is planned.

The scientific analysis will proceed as with IMP. Examination of the IMP images [*Smith et al.*, 1997a] showed a rock-strewn landscape that was entirely consistent with the expected flood plain for the Ares and Tiu Valles. Distant hills are layered and boulders are visible along terraces. South of the lander the rim of a large crater is visible, and several distant knobs are seen over the horizon. These features were used to exactly locate the lander in the Viking images [*Golombek et al.*, 1999]. Color differences are found in both the soils and the rocks although they are subtle variations on the goldenrod or butterscotch hue that characterizes Mars [*Maki et al.*, 1999; *McSween et al.*, 1999].

The polar layered terrain is expected to show clear evidence for the layering seen from orbit. Gentle slopes are expected to change color as they progress from one stratum to the next. Digging operations will be monitored to give a close-up spectral signature for any microlayers that may be found, and the tailings that are piled near the hole will also be examined for textural variations.

At the Viking 1 landing site, small ( $<25$ -m diameter) craters were much less numerous than expected by extrapolation of the size-frequency distribution derived from in-orbit remote sensing [*Binder et al.*, 1977]. *Arvidson et al.* [1979] estimated a regional erosion rate at this site of several meters over geological time that would be insufficient to explain this discrepancy.

The absence of small craters may be evidence that the atmosphere was previously denser than at present [Vasavada *et al.*, 1993]. At the polar layered terrain the surface is estimated to be young (tens of Ma), so the cratering density is low. Small craters may be visible, but no rocks are expected in this depositional terrain. The cratering record and potential ejecta blocks from distant impacts will be examined by the SSI to provide further constraints.

Aeolian processes are sure to have shaped the local topography, so it is very unlikely that the nearby surface will be flat and featureless. The Mars Orbiting Camera (MOC) images taken in August 1999 from Mars Global Surveyor show a bewildering diversity of small-scale topography, even when the area is still under a layer of frost. At the finest scale of resolution from MOC (M. Malin, private communication, 1999) there are north-south oriented linear features that may be yardangs. In addition, because the site is within the seasonal cap, many ice-forced surface-shaping processes will work to modify a flat surface; in turn, these will be eroded and reformed by the polar winds.

The color capability of the SSI will also be used to search for evidence of aeolian sorting on the surface. Small particles, stripped from dust layers by winds and deposited nearby, will lead to measurable changes in the surface photometry and will be particularly evident in the ratio of red and blue images of the surface. The SSI, especially in conjunction with RAC [Keller *et al.*, this issue], will therefore be able to identify relative changes in the surface particle size distribution.

The large dynamic range of the SSI allows a sensitive search for time variability of the surface features. At the extremes of low temperature in shaded pits and hollows, condensation of atmospheric volatiles may occur. A dedicated search for evidence of surface frosts during late night and morning hours will be performed. Viking 2 returned photographs of thin frost layers bright against the dusty surface, particularly at blue wavelengths. The monitoring of such time-variable features will provide data on the atmospheric and surface temperatures and the thermal inertia of the surface.

## 5. SSI Stereo Data Processing

The fundamental SSI camera product is a stereo image pair (or an "image cube" of pairs obtained with the same geometry but with different filters). By design, such a pair can be viewed directly to give a three-dimensional impression of a portion of the SSI landing site. In addition, quantitative photogrammetric processing is planned that will lead to several useful derived data products.

Following collection of a series of stereo image pairs by the SSI camera, a geometric control network will be established. Manual or semiautomatic collection of the locations of matching features between paired images will allow solution for the location of features in three dimensions. These solutions, in turn, will permit mosaicking of image sets without offsets at the seams.

Measurement of locations on the local horizon will allow conversion from the spacecraft-centered coordinates to local geographic coordinates. This type of match-point collection and solution for camera orientations will need to be performed at intervals during the mission, both because the camera platform pointing is not perfectly repeatable and because it indicates shifts in the lander's orientation. A similar matching process can use point measurements of distant landmarks that

are identifiable from orbit and in the descent images from MARDI in order to locate the landing site precisely. This technique has been applied successfully in the Surveyor, Apollo, Viking, and Pathfinder missions.

Once a control network has been established and camera orientations have been calculated, the next step is to match features in paired images on a point-by-point basis in order to determine the ranges to the features. In the current state of the art, the matching can be done automatically to an accuracy of  $\sim 0.2$  pixel of parallax though only as averaged over patches of the order of 5–10 pixels minimum width. The corresponding precision of depth measurements deteriorates linearly with range from the stereo baseline. On the other hand, the surface farther from the camera is viewed with increasing obliquity, so that the nominal precision in range (projected onto the ground) is everywhere about 2 pixels. Transverse resolution on nonhorizontal surfaces (e.g., facing surfaces of dunes or small hills) deteriorates less rapidly than the range resolution. By imaging such facing surfaces, it will be possible to make detailed fits of photometric functions (using local surface orientations from the stereo models) to determine surface scattering behavior.

These types of observations can be synergistic. For example, observations with multiple illumination angles will not only constrain the photometric function of surface regions but also can lead to higher spatial resolution modeling of the surface shape. Two-dimensional photoclinometry, or shape from shading [e.g., Kirk, 1987], can be used to recover geometric/topographic information at pixel scale, generating much more detail than stereo matching can. Such analysis relies on an accurate photometric function model, while images with multiple illumination conditions can be used to differentiate brightness differences due to shape and shading from those due to intrinsic albedo differences. A coarse shape model based on stereo matching is highly effective as a starting point for a photoclinometric solution [Giese *et al.*, 1996].

## 6. Multispectral Imaging

Multispectral views of the south polar region of Mars from Earth are historically limited by poor resolution since this region has not been visible during recent oppositions. The best ground-based visible and near-IR instruments produce image cubes with ground resolutions of hundreds of kilometers per pixel and Hubble Space Telescope (HST) cannot see down to the south pole because Mars in southern summer is near conjunction with the Sun. This large footprint averages large areas of potentially dissimilar materials and homogenizes the apparent surface mineralogy.

Little spectral diversity has been observed globally; there are three major spectral units: the gray, dark red, and bright red areas [Soderblom *et al.*, 1992]. The dark areas have a reflectance of about 15% in the red and near IR, while the light areas are approximately twice as bright in the same spectral region; the blue albedo is nearly constant over the planet except for regions covered by clouds, frost, or ice. Representative spectra of the two regions are shown by Soderblom *et al.* [1992]. Recently, HST has been able to spectrally map the planet at higher resolution [Bell *et al.*, 1997].

Both types of material show a strong absorption in the UV green (300–550 nm) that has been interpreted by many workers to be caused by the presence of oxidized iron. The spectra rise in the visible and plateau at  $\sim 700$  nm with a number of

weak absorption bands and shoulders. The spectral contrast of these features is low, owing either to low abundances of a divergent mineralogy or to a masking of spectral contrast by poorly crystalline weathering products or dust. In general, the spectra indicate the presence of both coarse and fine-grained iron oxides, basalts, pyroxenes of varying compositions, and as-yet-unidentified hydrated minerals. Less certain are the presence of carbonates, sulfates, carbonate- and sulfate-bearing minerals like scapolite, and clay silicate minerals like nontronite.

There is little hard data on the exact nature of the surface weathering processes, and the identification of these processes and of the mineralogy of their end products is a science goal. The weathering reactions probably involve water, oxygen, and carbon dioxide, supplemented by UV radiation, the diurnal and seasonal temperature cycles (over 100°C at the Polar Lander site), impact heating processes, and the abrasion of wind-blown dust. As the search for life on Mars intensifies, evidence for hydrothermal alteration becomes an important goal for all spectral studies, although this is not expected on the polar layered terrain.

A major science objective for the mineralogical filters is to obtain high-quality spectra of the different components that make up the polar layered terrain. No spectra exist of the horizontal layers that are distinguished from their slopes, their morphologies, and their albedos in red and blue light. The behavior of the spectra in the NIR may reveal absorptions shortward of 1  $\mu\text{m}$ ; any indication that ices are mixed into the soil can be detected as an anomalous brightening in the blue filter images. Changes of the red-to-blue ratio between layers indicate differences in the properties of the iron oxides that make up the soil strata. With luck we can examine both the trench walls and the material on the pile of excavated soil; these results will be compared with the unmodified surface units to determine the effects of weathering on the spectra.

### 6.1. SSI Spectral Operations

SSI can acquire multispectral image cubes consisting of up to 12 wavelengths, using the geology filters. The justification for the choice of filters, along with their expected diagnostic information, is identical with IMP and is given by *Smith et al.* [1997b, Table 4]. The band centers of the filters are clustered (profiles are shown in Figure 8) to optimize discrimination of the two most important mineral groups detectable by SSI. The first objective is to identify the crystalline ferric oxides, oxyhydroxides, and the poorly crystalline or nanophase ferric oxides [Morris and Lauer, 1990]. The major crystalline ferric oxide phases include hematite, goethite, maghemite, magnetite, and lepidocrocite [Morris et al., 1985]. The basaltic weathering product palagonite is an example of a material that has visible to near-IR spectral properties dominated by nanophase ferric oxides [Morris et al., 1989, 1990]. The spectrally diagnostic region for these minerals is primarily in the 440- to 860-nm range using eight of the filters. This allows for discrimination based on four spectral parameters: (1) the position of the ferric iron UV drop-off (diagnostic of goethite, maghemite, magnetite, and lepidocrocite); (2) the position of the electronic transition band near 860 nm (diagnostic of hematite, goethite, and maghemite); (3) the presence of an electronic transition band near 650 nm; and (4) the presence of a feature between 650 and 800 nm. The depth of features at these diagnostic band passes can provide information on the crystallinity of the target material.

### 6.2. SSI Calibration Target Description

Calibration targets for SSI provide a direct reflectance standard [Smith et al., 1997b; Reid et al., 1999]. There are two types of calibration targets: color targets, which aid color balancing for true color images and provide a direct comparison of object and target for three iron oxides, and a radiometric target (RT), which permits radiometric calibration of scene elements. The calibration targets were made by direct casting of various pigments in a silicone binder; they were cast in aluminum molds with a bead-blasted surface that is nearly Lambertian. Targets were then "preyellowed" by ultraviolet exposure until the spectral behavior stabilized.

The pigments for the five colors comprise three pure iron oxides, hematite (also provides red color reference), maghemite, and goethite, and two additional color reference targets, green (chromium dioxide paint pigment) and blue (cobalt blue paint pigment). The color targets were cut from the same castings as the IMP color targets and have identical reflectance properties. Reflectance spectra of the color targets are given by *Smith et al.* [1997b, Figures 9 and 10]; they were not remeasured for MVACS. The hematite color chip was mistakenly installed on the Pathfinder upside-down, leaving the shiny surface exposed; this results in a brighter spectrum than expected due to differences in albedo between the two sides of the target.

The RT consists of a white, gray, and black ring, with a shadow post at the center. Pigments used for the radiometric targets were rutile (white), carbon black (black), and a mixture of rutile and carbon black (gray). The RT has a reflectance spectrum nearly identical to the IMP RTs [Smith et al., 1997b, Figure 11].

Reflectance characteristics of the SSI RT were measured at the German Aerospace Research Establishment (DLR) in Berlin. The DLR measurements were made at a range of geometries ( $i = 0^\circ\text{--}50^\circ$ ,  $e = 26^\circ$ ,  $az = 0^\circ\text{--}180^\circ$ ), improving on the single geometry used for IMP targets. Using the DLR data should improve absolute, relative, and eye-to-eye calibration since the true reflectivity of the RT can be determined for arbitrary photometric geometries. However, limitations in the DLR goniometer restricted it to  $<50^\circ$  incidence angle, and the incidence angle at the MPL landing site will usually be  $>50^\circ$ . So, extrapolation using data from the DLR measurements of the IMP RTs will be necessary.

The baseline technique for calibrating scene images relative to the RTs derives from the target calibration algorithm (SPECTCAL) used to calibrate IMP image data [Reid et al., 1999]. In order to correct scene radiance in units of DN/s to reflectance, a transfer function must be created by fitting the measured target radiances to the laboratory-measured target reflectances. The calibration algorithm forces zero reflectance to equal 0 DN/s and weighs the white and gray targets roughly equally, ignoring the black target, which has large systematic uncertainty. The new transfer function is derived from Reid [1997].

Ideally, the observation of the RT will occur concurrently with the acquisition of the multispectral images. In general, however, this may not be the case. For Pathfinder an accurate atmosphere model [Tomasko et al., 1999; Markiewicz et al., 1999] allowed the total direct solar plus diffuse sky flux to be determined at different times of day, permitting scaling of the RT measurements to the effective radiance concurrent with scene images. Scaling to the same time of day can be an

important factor (as large as 20%) in the determination of absolute reflectance of the surface as well as a smaller (~2%) effect on the relative reflectance due to the variation in color of the sky illumination [Yingst *et al.*, 1999].

Dust accumulation at the MPF landing site was measured to be ~0.25%/sol from IMP images of the RT [Smith *et al.*, 1998] and 0.28%/sol by a materials adherence experiment [Rover Team, 1997]. As dust accumulates, the black target (nominally ~4% reflective) brightens, and the white target (nominally ~96% reflective) darkens. Dust accumulation as measured by the ratio of the black to white targets will be modeled and tracked throughout the mission. The dust signature must be taken into account when interpreting calibration relative to the targets, especially later in the mission as dust accumulation becomes significant.

The most significant factor that complicates calibration to absolute reflectance is the balance and spatial distribution of direct and diffuse illumination on both the surface and the RTs. Laboratory reflectance measurements are generally quantified in terms of bidirectional reflectance; that is, a single collimated beam illuminates the object at a fixed incidence angle, which is observed at a single emission angle. On Mars the solar illumination geometry changes with each observation. Furthermore, significant atmospheric opacity is expected (~0.5 for MPF [Smith and Lemmon, 1999]), so that the amount of illumination from the sky can be 50% of the total irradiance on the surface. While a first-order separation of solar and atmospheric illumination can be performed on the RTs by measuring the radiance in both the shaded and sunlit portions of the target, they cannot be easily separated on Martian surface materials without an understanding of the photometric and topographic properties of the surface. The result of the target calibration has therefore been termed  $R^*$ , defined as the total measured radiance of the surface divided by the total measured radiance of the RT scaled to its equivalent Lambert brightness [Reid *et al.*, 1999]. This is conceptually similar to the radiance coefficient as defined by Hapke [1981] but is not a true measurement of bidirectional reflectance.

## 7. Studies of Aerosols and Water Vapor

The dust in the Martian atmosphere has been shown to play a crucial role in many atmospheric processes [Pollack *et al.*, 1979] affecting the absorption of solar energy and the emission of thermal infrared radiation. Hence the thermal structure of the atmosphere depends on the dust loading, the size of the particles, and their optical properties. The radiative heating and cooling both depend on the dust and alter the forcing for atmospheric dynamics. Surface interactions varying from local dust devils of short duration to dust storms that are essentially global and last for weeks have been observed. The dust in the atmosphere provides nuclei for condensation of water ice and even carbon dioxide ice at various altitudes and locations. In the polar regions, carbon dioxide ice can nucleate and grow to large sizes. Their precipitation out of the atmosphere is an important mechanism for removing dust from the atmosphere and depositing it, along with the ices, in the polar caps. In view of the large roles played by the dust and ice particles in the thermal balance, dynamics, and water and carbon dioxide transport, it is important to have an accurate picture of the distribution and properties of the dust and ice crystals at various times of day and year at many locations over the planet.

At a given location the dust distribution can be characterized

by number density as a function of altitude, the mean effective radius of the dust particles, their real and imaginary refractive indices as functions of wavelength, and additional parameters that govern the shape of the single-scattering phase function. For dust particles that are expected to be nonspherical, these additional parameters have been described by Pollack and Cuzzi [1980] and Showalter *et al.* [1992].

Thus our science goals are to determine (1) the aerosol optical depth (as a function of wavelength) above the landing site; (2) the effective size and number density of the atmospheric aerosols; (3) several parameters characterizing the shape of the aerosol particles; (4) the vertical distribution of the aerosols; and (5) the imaginary refractive index of the aerosol particles. When both dust and ice particles are present, we plan to distinguish between them on the basis of their absorption properties as a function of wavelength. Finally, we plan to measure the variations in the aerosol properties with time by making regular observations throughout the mission.

### 7.1. Reduction and Analysis of Aerosol Observations

The aerosol optical depth will be calculated from the ratios of the flux from the Sun obtained through different air masses. A subframe (30 × 30 pixels) centered on the solar disk is returned for each observation, the background due to the surrounding sky brightness is subtracted, and the pixels covering the solar disk are summed. When multiple scattering is negligible, the variation of flux from the external source obeys Beer's law, and the log of the ratio of intensities observed at two solar zenith angles divided by the difference of their secants gives the vertical optical depth of the aerosols. Departures from Beer's law at different times of day (after correction for the small effects of multiple scattering) indicate changes in the vertical optical depth of the aerosols at the wavelength of the measurement. Color observations are able to distinguish between the clouds and the dust. Viking imaging determined dust optical depths from a few tenths to values >5 during global dust storms; however, their observations were limited to angles near the horizon, and they could observe the Sun only in the red. Pathfinder [Smith and Lemmon, 1999] observed the optical depths increasing throughout the 83-sol mission from 0.4 to 0.6 with considerable diurnal variability.

The width of the forward scattering portion of the single-scattering phase function is controlled by diffraction and is determined by the projected area of the particles with little sensitivity to particle shape. Measurements of the variation of the sky intensity with azimuth when the Sun was low in the sky were used by Viking and Pathfinder to constrain the mean effective dust particle radius [Pollack *et al.*, 1995; Tomasko *et al.*, 1999]. We will observe the solar aureole at various other times of the day. The data will be collected at several wavelengths between 0.4 and 1.0  $\mu\text{m}$  to provide a consistency check of the particle size and to determine the absorptivity of the aerosols.

Once the extinction optical depth as a function of wavelength is known, along with information on the shape of the phase function from the solar aureole (including sidescattering and backscattering observations), the size and cross section of the aerosol particles can be estimated. Division of the optical depth by the average cross section gives the particle number density. Note that the optical depth as a function of wavelength provides an important consistency check on the particle size and shape, as the observations at each optical depth must give

a consistent number density from the extinction data at all wavelengths.

## 7.2. Measurements of the Abundance of Water Vapor

The amount of water vapor in the atmosphere of Mars is known to vary significantly with time of day, location, and season [Jakosky and Farmer, 1982]. Understanding the transport of water in the Martian atmosphere is a prerequisite for understanding the current and past climate of Mars and the evolution of the planet to its current state.

The brightness of the Sun in a 5-nm-wide water band will be measured. Figure 14 of Smith *et al.* [1997b] indicates the transmission of the atmosphere as a function of water content at 10 air masses (86° solar zenith angle) using line-by-line calculations based on the Air Force Geophysics Laboratory (AFGL) line list. The figure includes variations of a factor of 3 around the nominal water content of 10 precipitable  $\mu\text{m}$ . Absorptions of several percent will occur under these conditions. At 10 air masses, measurements with good signal to noise ( $\geq 1000$ ) provide good determinations of water vapor for modest dust abundances [Titov *et al.*, 1999]. SSI will achieve higher signal to noise than Pathfinder because the SSI measurements will be able to be flat field corrected; lack of ability to do such a correction (due to inability to determine from where on the CCD the subframe containing the Sun image was taken) added a 1% uncertainty to each of the solar images taken by Pathfinder.

It is important that the continuum filter be sufficiently close in wavelength to the water band filter so the variation in optical properties of the dust between the two filters is small. In Table 5, three continuum filters are listed (883, 925, and 989 nm), and a quadratic fit to the three intensity values allows an accurate measure of the continuum at the wavelengths of the water bands. Three water band filters are provided: two narrow (935 nm, left and right eyes) and one broadband (945 nm).

The measurements consist of image pairs of the Sun in the three 5-nm-wide filters obtained at the lowest Sun elevations. In addition, special care has been taken to control the temperature of the detector (heated to  $T = -20^\circ\text{C}$ ) during these observations to reduce variations due to changes in the relative response near the long wavelength end of the silicon CCD response. With stable temperatures, systematic effects can be kept to low levels, and random noise is expected to dominate the accuracy of the water vapor determination. Uncertainty in the position of the Sun on the CCD, and the resulting uncertainty in the flat field correction, was the dominant source of uncertainty for IMP water measurements [Titov *et al.*, 1999]. For SSI we will know the position of the Sun on the CCD for all downlinked images.

## 8. Summary

The SSI camera, a clone of the IMP camera on Pathfinder, has been described in terms of both its physical properties and its performance. Emphasis is given to areas where the two cameras differ. The IMP camera was  $\sim 30\%$  more responsive than SSI; this is attributed to a 15% smaller aperture diameter in the lens cell. On the other hand, the pointing repeatability has been improved for the SSI by a redesign of the AZ/EL gearheads. Otherwise, the cameras are similar in all respects.

The scientific goals for SSI fall into five general areas: atmospheric studies, topographic mapping using stereoscopic views, multispectral imaging normalized to a target of known

reflectance, and true color mosaics. An additional goal of studying the magnetic properties of airborne dust will be discussed in a separate paper [Tilsted Mogensen *et al.*, this issue].

The true panoramic and stereoscopic views will be obtained together during sols 1–3 of the mission. These data represent mission success for the SSI and can be used for interpreting the local geology, making topographic maps, supporting public outreach with imaging products, and planning multispectral observations on the basis of color and morphology.

The multispectral data set will start with a stripe across the scene on sol 1 and build with a selection of subframed multispectral images on interesting targets during the first few weeks. As the data volume becomes available during the mission, we will attempt a complete panorama with 15 filters and low compression (12 color, three stereo pairs). Each observation is calibrated with views of the radiometric target, a copy of the Pathfinder targets.

Finally, views of the solar disk through narrowband, low-transmission filters and of the sky through the regular filters give us a wealth of information concerning haze and cloud properties. Smith and Lemmon [1999] analyzed the haze and cloud optical depth measurements throughout the Pathfinder mission. From integrated solar disk values, time history of the opacity changes could be told. Using the optical depth as an input parameter, Tomasko *et al.* [1999] and Markiewicz *et al.* [1999] analyzed sky data at constant elevation with a low Sun and near noon with a vertical meridional scan, respectively. Their results show how well aerosol properties can be constrained with a simple filter radiometer.

Several filters in and around the 938-nm water vapor band are used to constrain the water vapor content of the atmosphere. Titov *et al.* [1999] conducted a thorough analysis for Pathfinder data. The experiment on Pathfinder was hampered because the subframe location necessary for flat field correction was not downlinked for most data sets. This situation has been corrected for SSI.

During cruise the SSI performed nominally; all dark current data returned are within specification. As expected, a few percent of pixels have been affected by the radiation environment during cruise. The instrument was in top condition before its date with Mars. We deeply regret its loss.

**Acknowledgments.** Developing a camera concept into a space-flight-ready instrument requires the concerted efforts of a large number of dedicated people and the support of many organizations. We have the pleasure to have worked with many talented individuals and are deeply grateful for their fine efforts. Local engineering support at the UA was provided by Steve Bell and Dennis Bowers in electronics, Devon Crowe in calibration, and Chris Shinohara in software. In addition, the project could not have proceeded without the support of Mary Williams in the project office. The JPL project office, led by Young Park, provided the services of Barry Goldstein, Robert Denise, and Raul Romero to guide the integration and testing during all stages of the project; David Paige and his hardworking team at UCLA were very helpful throughout the project. The hardware development at MP Ae was managed by Detlef Koschny; K. Eulig, J. Nitsch, H. Hartwig, and H. Schuddekopf helped with CCD characterization. We thank J. F. Bell and S. Murchie for their reviews.

## References

- Arvidson, R. E., E. A. Guinness, and S. Lee, Differential aeolian redistribution rates on Mars, *Nature*, 278, 533, 1979.
- Bell, J. F., III, M. J. Wolff, P. B. James, R. T. Clancy, S. W. Lee, and L. J. Martin, Mars surface mineralogy from Hubble Space Telescope

- imaging during 1994–1995: Observations, calibration, and initial results, *J. Geophys. Res.*, **102**, 9109–9123, 1997.
- Binder, A. B., R. E. Arvidson, E. A. Guinness, K. L. Jones, E. C. Morris, T. A. Mutch, D. C. Pieri, and C. Sagan, The geology of the Viking Lander 1 site, *J. Geophys. Res.*, **82**, 4439–4451, 1977.
- Boynton, W., et al., Thermal Evolved Gas Analyzer: Part of the Mars Volatile and Climate Surveyor integrated payload, *J. Geophys. Res.*, this issue.
- Giese, B., G. Oberst, R. Kirk, and W. Zeitler, The topography of asteroid Ida: A comparison between photogrammetric and two-dimensional photoclinometric image analysis, *Proc. Int. Soc. Photogramm. Remote Sens.*, **XVIII**, 1996.
- Golombek, M. P., et al., Overview of the Mars Pathfinder mission: Launch through landing, surface operations, data sets, and science results, *J. Geophys. Res.*, **104**, 8523–8553, 1999.
- Hapke, B., Bidirectional reflectance spectroscopy, 1, Theory, *J. Geophys. Res.*, **86**, 3039–3054, 1981.
- Jakosky, B. M., and C. B. Farmer, The seasonal and global behavior of water vapor in the Mars atmosphere: Complete global results of the Viking atmospheric water detector experiment, *J. Geophys. Res.*, **87**, 2999–3019, 1982.
- Keller, H. U., et al., The MVACS Robotic Arm Camera, *J. Geophys. Res.*, this issue.
- Kirk, R. L., A fast finite-element algorithm for two-dimensional photoclinometry, Ph.D. dissertation, pp. 165–258, Calif. Inst. of Technol., Pasadena, 1987.
- Kramm, J. R., N. Thomas, H. U. Keller, and P. H. Smith, The CCD imager electronics for the Mars Pathfinder and Mars Surveyor cameras, *IEEE Trans. Instrum. Meas.*, **47**(5), 1112–1118, 1998.
- Madsen, M. B., S. F. Hviid, H. P. Gunnlaugsson, J. M. Knudsen, W. Goetz, C. T. Pedersen, A. R. Dinesen, C. T. Mogensen, M. Olsen, and R. B. Hargraves, The magnetic properties experiments on Mars Pathfinder, *J. Geophys. Res.*, **104**, 8761–8779, 1999.
- Maki, J. N., J. J. Lorre, P. H. Smith, R. D. Brandt, and D. J. Steinwand, The color of Mars: Spectrophotometric measurements at the Mars Pathfinder landing site, *J. Geophys. Res.*, **104**, 8781–8794, 1999.
- Markiewicz, W. J., R. M. Sablotny, H. U. Keller, and N. Thomas, Optical properties of the Martian sky as derived from Imager for Mars Pathfinder midday sky brightness data, *J. Geophys. Res.*, **104**, 9009–9017, 1999.
- McSween, H. Y., Jr., et al., Chemical, multispectral, and textural constraints on the composition and origin of rocks at the Mars Pathfinder landing site, *J. Geophys. Res.*, **104**, 8679–8715, 1999.
- Mogensen, C., J. M. Knudsen, M. B. Madsen, P. Bertelsen, S. F. Hviid, R. B. Hargraves, P. H. Smith, and D. A. Paige, Magnetic Properties Experiments on the Mars Polar Lander, *J. Geophys. Res.*, this issue.
- Morris, R. V., and H. V. Lauer, Matrix effects for reflectivity spectra of dispersed nanophase (superparamagnetic) hematite with application to Martian data, *J. Geophys. Res.*, **95**, 5101–5109, 1990.
- Morris, R. V., H. V. Lauer Jr., C. A. Lawson, E. K. Gibson Jr., G. A. Nace, and U. Stewart, Spectral and other physicochemical properties of submicron powders of hematite, maghemite, magnetite, goethite, and lepidocrocite, *J. Geophys. Res.*, **90**, 3126–3144, 1985.
- Morris, R. V., D. G. Agresti, H. V. Lauer Jr., J. A. Newcomb, T. S. Shelfer, and A. V. Murali, Evidence for pigmentary hematite on Mars based on optical, magnetic and Mossbauer studies of superparamagnetic (nanocrystalline) hematite, *J. Geophys. Res.*, **94**, 2760–2778, 1989.
- Morris, R. V., J. L. Gooding, H. V. Lauer, and R. B. Singer, Origins of the Mars-like spectral and magnetic properties of a Hawaiian palagonitic soil, *J. Geophys. Res.*, **95**, 14,427–14,434, 1990.
- Pollack, J. B., and J. N. Cuzzi, Scattering by nonspherical particles of size comparable to a wavelength: A new semi-empirical theory and its application to tropospheric aerosols, *J. Atmos. Sci.*, **37**, 868–881, 1980.
- Pollack, J. B., D. S. Colburn, F. Michael, R. Kahn, C. E. Carlston, and D. Pidek, Properties and effects of dust particles suspended in the Martian atmosphere, *J. Geophys. Res.*, **84**, 2929–2945, 1979.
- Pollack, J. B., M. E. Ockert-Bell, and M. K. Shepard, Viking Lander image analysis of Martian atmospheric dust, *J. Geophys. Res.*, **100**, 5235–5250, 1995.
- Reid, R. J., Spectrophotometric calibration of Imager for Mars Pathfinder datasets, thesis, Univ. of Ariz., Tucson, 1997.
- Reid, R. J., et al., Imager for Mars Pathfinder (IMP) image calibration, *J. Geophys. Res.*, **104**, 8907–8926, 1999.
- Reynolds, R. O., P. H. Smith, L. S. Bell, and H. U. Keller, The design of Mars Lander cameras for Mars Pathfinder, Mars Surveyor '98, and Mars Surveyor '01, *IEEE Trans. Instrum. Meas.*, **50**, 63, 2001.
- Rover Team, Characterization of the Martian surface deposits by the Mars Pathfinder rover, Sojourner, *Science*, **278**, 1765–1768, 1997.
- Rueffer, P., F. Rabe, and F. Gliem, Enhancement of IMP lossy image data compression using LCT, in *Space and Earth Science Data Compression Workshop*, *JPL Publ.*, **95-8**, 120, 1995.
- Showalter, M. R., J. B. Pollack, M. E. Ockert, L. R. Doyle, and J. B. Dalton, A photometric study of Saturn's F ring, *Icarus*, **100**, 394–411, 1992.
- Smith, P. H., and M. T. Lemmon, Opacity of the Martian atmosphere measured by the Imager for Mars Pathfinder, *J. Geophys. Res.*, **104**, 8975–8985, 1999.
- Smith, P. H., et al., Results from the Mars Pathfinder camera, *Science*, **278**, 1758–1765, 1997a.
- Smith, P. H., et al., The Imager for Mars Pathfinder experiment, *J. Geophys. Res.*, **102**, 4003–4025, 1997b.
- Smith, P. H., M. T. Lemmon, and M. G. Tomasko, The dust cycle observed by Pathfinder (abstract), *Bull. Am. Astron. Soc.*, **30**, 1022, 1998.
- Soderblom, L. A., The composition and mineralogy of the Martian surface from spectroscopic observations: 0.3  $\mu\text{m}$  to 50  $\mu\text{m}$ , in *Mars* edited by H. H. Kieffer et al., pp. 557–593, Univ. of Ariz. Press, Tucson, 1992.
- Thomas, N., W. J. Markiewicz, R. M. Sablotny, M. W. Wuttke, H. U. Keller, J. R. Johnson, R. J. Reid, and P. H. Smith, The color of the Martian sky and its influence on the illumination on the Martian surface, *J. Geophys. Res.*, **104**, 8795–8808, 1999.
- Titov, D. V., W. J. Markiewicz, N. Thomas, H. U. Keller, R. M. Sablotny, M. G. Tomasko, M. T. Lemmon, and P. H. Smith, Measurements of the atmospheric water vapor on Mars by the Imager for Mars Pathfinder, *J. Geophys. Res.*, **104**, 9019–9026, 1999.
- Tomasko, M. G., L. R. Doose, M. Lemmon, P. H. Smith, and E. Wegryn, Properties of dust in the Martian atmosphere from the Imager on Mars Pathfinder, *J. Geophys. Res.*, **104**, 8987–9007, 1999.
- Vasavada, A. R., T. J. Milavec, and D. A. Paige, Microcraters on Mars: Evidence for past climatic variations, *J. Geophys. Res.*, **98**, 3469–3476, 1993.
- Yingst, R. A., R. J. Reid, P. H. Smith, and J. W. Rice Jr., Preliminary science results from the recalibration of IMP images (abstract), paper presented at 5th International Mars Conference, Pasadena, Calif., 1999.

B. J. Bos, T. Friedman, M. T. Lemmon, R. L. Marcialis, C. Oquest, R. J. Reid, R. Reynolds, P. H. Smith, R. Tanner, and J. Weinberg, Lunar and Planetary Laboratory, University of Arizona, 1629 East University Avenue, Tucson, AZ 85721. (psmith@lpl.arizona.edu)  
 F. Gliem and P. Rueffer, Technical University of Braunschweig, Braunschweig, Germany.  
 H. U. Keller, R. Kramm, and W. J. Markiewicz, Max Planck Institute for Aeronomy, Katlenberg-Lindau D-3411, Germany.

(Received June 11, 1999; revised November 15, 1999; accepted December 6, 1999.)